TICRA

Reflector surface model investigation

ACE deliverable 2.3D4

Editor: Knud Pontoppidan

December, 2005 S-1268-02

TICRA
LÆDERSTRÆDE 34 · DK-1201 COPENHAGEN K DENMARK
TELEPHONE +45 33 12 45 72 TELEFAX +45 33 12 08 80
E-MAIL ticra@ticra.com http://www.ticra.com

VAT REGISTRATION NO. DK-1055 8697
TICRA FOND, CVR REG. NO. 1055 8697

TABLE OF CONTENTS

1. Introduction 1

1. Introduction

The present report describes the activities carried out in WP2.3-2, Reflector Surface Models, in the last year of ACE1. The report is organised in the following eight chapters where the name of the contributing organisation is given in parentheses:

1. Introduction (TICRA)
2. Range of validity of boundary conditions obtained by homogenization method (Chalmers)
3. Range of validity of canonical homogenised problems and
   Effects of manufacturing tolerances (Univ. Lund)
4. Test case, Multi-layer frequency selective surface, Parametric analysis of the effects of manufacturing tolerances (TNO)
5. Effects from manufacturing tolerances (POLITO)
6. Fast approximate methods compared to rigorous solutions (TICRA)
7. The Pole-Zero Matching Method applied to the frequency selective radome (univ. Siena)

Homogenisation problems are dealt with in both chapters 2 and 3. The general idea is to replace the original inhomogeneous medium with a homogeneous one with the same electromagnetic properties. In chapter 2 the method is applied to a two-dimensional strip grid and it is demonstrated that the approach works well, not only for planar structures, but also for cylindrical structures with diameters of only a few wavelengths.

The general homogenisation for three-dimensional media are described in the first half of chapter 3 and it is indicated under which conditions the equivalent homogeneous material exists.

The second half of chapter 3 deals with the influence of manufacturing tolerances which is also the subject of chapters 4 and 5. In chapter 3 the investigation is concentrated to a frequency selective (FSS) radome and in chapter 4 a planar FSS test case is investigated, both numerically and experimentally. In chapter 5 the misalignment of the elements forming the FSS grid is examined.

Chapter 6 is devoted to strip grids and gives a comparison between fast, but approximate formulas and rigorous results obtained by Moment Methods. It is concluded that the simple formulas work very well in general, but when the strip grid is located very close to a dielectric interface unacceptable errors show up.

Chapter 7 describes the preliminary work of a new method, the Pole-Zero Matching (PZM) Method. The general idea is to develop intelligent interpolation techniques such that rigorous, but CPU-time heavy, results can be implemented in realistic and fast optimisation procedures. One example is the PZM where the complicated frequency dependence of frequency selective surfaces is approximated by a simple rational function.

2. Range of validity of boundary conditions obtained by homogenization method

2.1 Planar structures

Analysis method: Strip gratings are well known for their polarization properties. Incident waves with the electric field parallel to the strips are mainly reflected, and waves with the electric field orthogonal to the strips mainly pass through the grating. In the present section we discuss the accuracy of two approximate boundary conditions which implementation significantly simplify the analysis of structures with strips. We consider strip gratings located in free space or placed on dielectric slab (Fig. 1). The analysis can be easily extended for strips located between any two layers inside cylindrical multilayer structures. Furthermore, we are interested in both planar and curved structures. As a canonical example of curved structures, strips located on dielectric cylinder are analyzed.

The rigorous analysis of periodic strips inside a multilayer structure is performed by expanding the currents on the strips in basis functions, and the amplitudes of the basis functions are determined numerically by the moment method (MoM) [1]. The electromagnetic field is in the form of Floquet modes due to the periodicity of the structure. It is sufficient to determine the current on one strip, since the currents on the other strips are identical except for a phase difference.

If the source excites a full spectrum of plane waves, such as a dipole, the Floquet-mode expansion/MoM is a laborious process. A simpler approach is to use approximate boundary conditions. We have used two types of approximate boundary conditions: the asymptotic strip boundary conditions (ASBC) [2], [3] which in the planar case correspond to modeling the strips as a unidirectional conducting screen [4], and boundary conditions obtained by the homogenization method (BCHM).

The ASBC are applied to the components of the electromagnetic field that are tangential to the interface which contains the strips. The electric field component parallel to the strips is zero at the strip surface, and the component orthogonal to the strips is continuous across the surface. For the magnetic field it is sufficient to consider the component

parallel to the strips, which is continuous across the surface. The orthogonal component is discontinuous by the amplitude of the strip current, which comes out as a result of the analysis. For *y*-directed strips the ASBC are

$$E_y^+ = 0\,, \qquad E_y^- = 0\,, \tag{1a}$$

$$E_x^+ = E_x^-\,, \qquad H_y^+ = H_y^-\,, \tag{1b}$$

where superscripts + and - denote the E- and H-fields and permittivity/permeability above and below the strips, respectively.

BCHM are obtained by averaging the fields of the fundamental Floquet mode [5]. The zero-order boundary conditions correspond to ASBC, and the first-order boundary conditions include the periodicity and the width of the strips. For example, for *y*-directed strips we have

$$E_x^+ = E_x^-\,, \quad E_y^+ = E_y^-\,, \tag{2a}$$

$$E_y = \frac{l_e}{2}\left[j\omega \frac{2\mu^+\mu^-}{\mu^+ + \mu^-}(H_x^+ - H_x^-) + \frac{2}{\varepsilon^+ + \varepsilon^-}\frac{\partial}{\partial y}(\varepsilon^+ E_z^+ - \varepsilon^- E_z^-) \right] \tag{2b}$$

$$H_y^+ - H_y^- = 2l_h\left[-j\omega \frac{\varepsilon^+ + \varepsilon^-}{2} E_x + \frac{\mu^+ + \mu^-}{2\mu^+\mu^-}\frac{\partial B_z}{\partial y} \right] \tag{2c}$$

Parameters l_e and l_h are defined by

$$l_e = \frac{P}{\pi}\ln\csc\frac{\pi W}{2P}\,, \quad l_h = \frac{P}{\pi}\ln\sec\frac{\pi W}{2P}\,, \tag{3}$$

where P and W are the periodicity and the width of the strips (Fig. 1). Notice that BCHM are more complicate to implement since the normal components of the electromagnetic field is also included in BCHM, which was not the case for ASBC. Furthermore, the ASBC can be obtained from BCHM by letting $P \to 0$ and by keeping the ratio P/W constant.

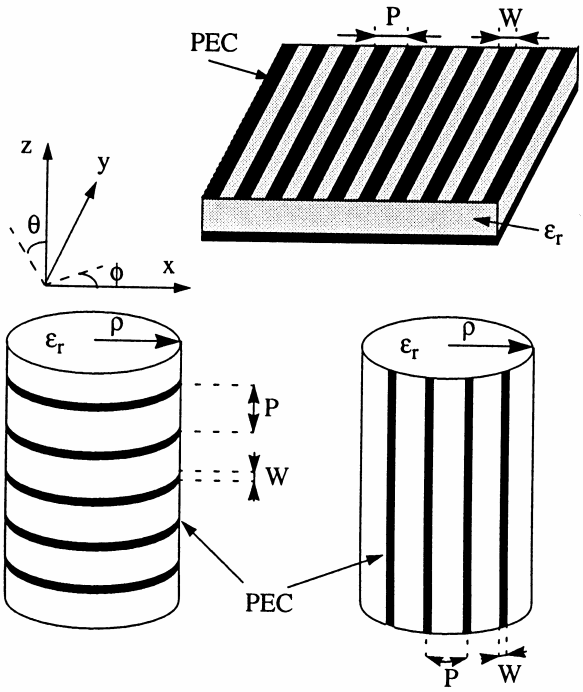

Figure 1. Geometry and coordinates of strip grids on a planar dielectric slab (up) and on dielectric cylinder with circular cross-section (down). The analysis in the present paper can also treat strip grids located inside multilayer planar and cylindrical structures.

Results: We consider here a planar strip grid, and we calculate the reflection coefficient for different strip widths, strip periodicities and angles of incidence. First we analyze the case when the strips are *y*-directed (see Fig. 1) and the incident wave is propagating orthogonal to the strips ($\varphi^{inc} = 0^0$). Fig. 2 shows the results for the case when the strip grid is in the free-space and we vary the strip period (the width of the strips is W/P = 0.25 λ_0 and θ^{inc} is a parameter). The results show that the ASBC act as a PEC plane or as a completely transparent surface, depending on polarization. The MoM results approach asymptotically the results obtained by the ASBC method when the strip periods decrease. Furthermore, the ASBC are better closer to grazing incidence. The comparison of the BCHM and the MoM results for the same case is given in Fig.3. It can be seen that the BCHM results are almost identical to the MoM results. However, the BCHM are harder to implement.

The strip-loaded grounded dielectric slab can be used as a soft surface, i.e. as a surface for which the reflection coefficient is independent of polarization: $\Gamma_{TE} = \Gamma_{TM} = -1$ [6]. Fig. 4 shows the dependence of the phase of the reflection coefficient on frequency when the strip width is parameter. The relative permittivity of the substrate is $\varepsilon_r = 2.5$ and the strip periodicity P is equal to the thickness of the slab d, $P = d$. As in the previous example the incident wave is propagating orthogonal to the strips ($\varphi^{inc} = 0^0$). The results again show that the MoM results approach the ones obtained by ASBC when the periodicity goes to zero for all relative strip widths. In the case of TE_z incident wave, when the strips act like a PEC plane, the ASBC are a better approximation the wider the strips are, and in the TM_z case the narrower the strips are. The MoM results also show a fast change of phase for the TE_z case when the thickness of the slab is around d = 0.32 λ_0 and the strip width is small compared to the period. We explain this

as excitation of a parallel-plate TE_z waveguide mode in the strip-loaded dielectric slab, having a cosine field distribution between the ground plane and the strip grating. The ASBC cannot predict such resonance-like phenomena. Here we did not present the BCHM results since they are almost identical to the MoM ones.

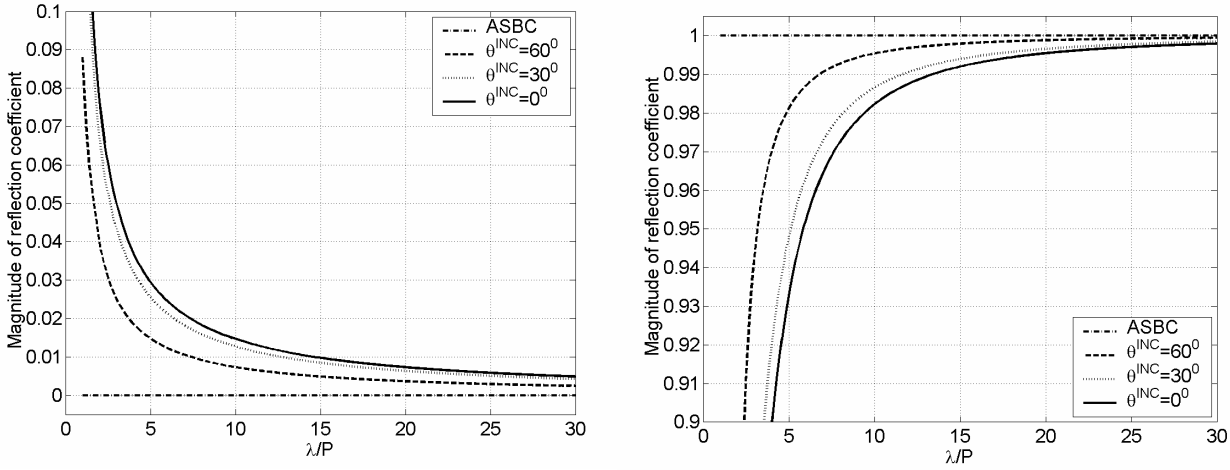

Figure 2. Absolute value of the reflection coefficient of a planar *y*-directed strip grid for transverse incidence for $W/P = 0.25$.

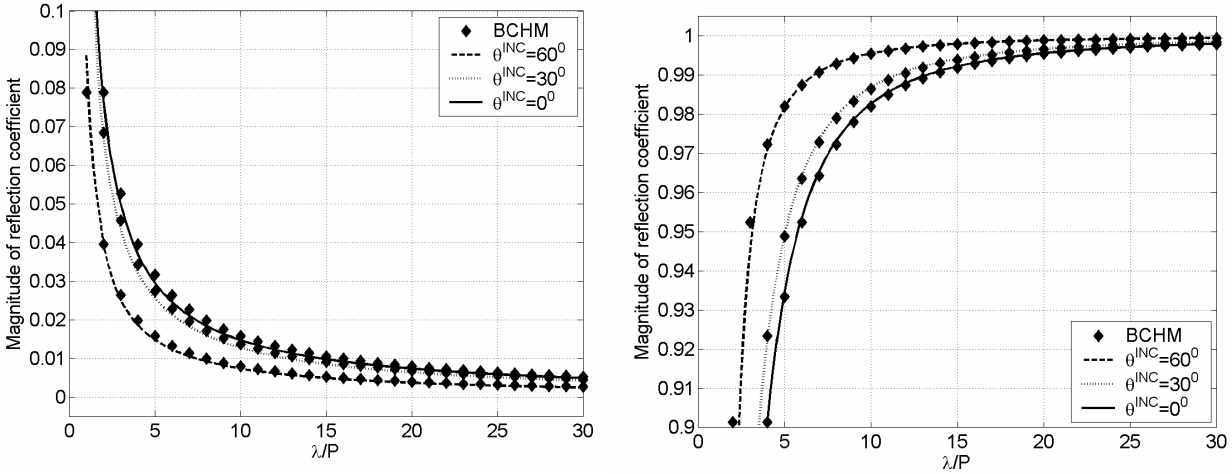

Figure 3. Absolute value of the reflection coefficient of a planar *y*-directed strip grid for transverse incidence for $W/P = 0.25$.

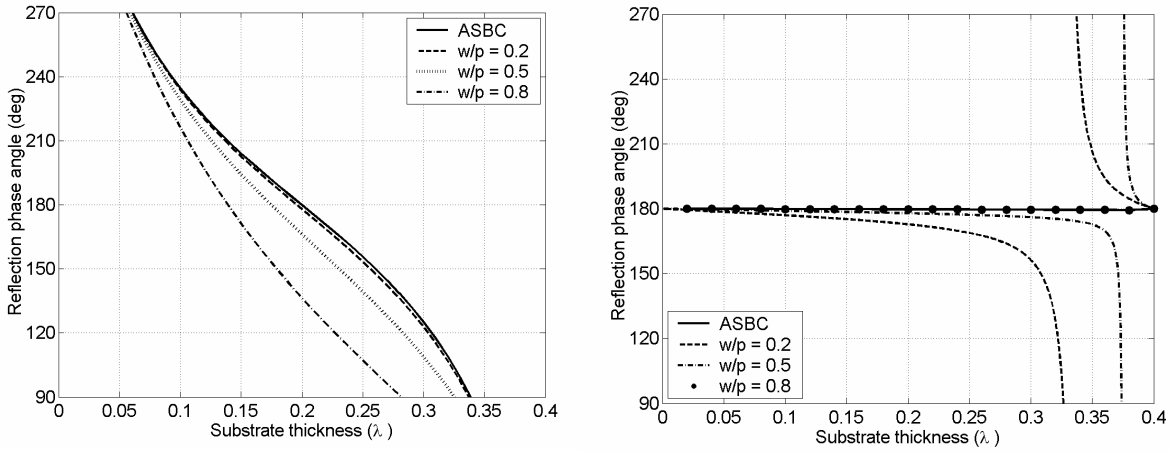

Figure 4. Phase of reflected field from a grounded dielectric slab loaded with *y*-directed periodic strips. $\theta^{inc} = 75^0$, $\varphi^{inc} = 0^0$, $\varepsilon_r = 2.5$, $P = d$.

2.2 Curved structures

In the BCHM case we have used a local planar approximation, that means we suppose that the surface where the strips are located is locally a plane surface. By this we can easily transform the boundary conditions from the rectangular coordinate system [5] to the cylindrical one. For example, for φ-directed strips we have

$$E_\phi^+ = E_\phi^- \ , \quad E_z^+ = E_z^- \ , \tag{4a}$$

$$E_\phi = -\frac{l_e}{2}\left[j\omega \frac{2\mu^+\mu^-}{\mu^+ + \mu^-}(H_z^+ - H_z^-) - \frac{2}{\varepsilon^+ + \varepsilon^-}\frac{1}{\rho}\frac{\partial}{\partial\phi}(\varepsilon^+ E_\rho^+ - \varepsilon^- E_\rho^-)\right] \tag{4b}$$

$$H_\phi^+ - H_\phi^- = 2l_h\left[j\omega \frac{\varepsilon^+ + \varepsilon^-}{2} E_z + \frac{\mu^+ + \mu^-}{2\mu^+\mu^-}\frac{1}{\rho}\frac{\partial B_\rho}{\partial\phi}\right] \tag{4c}$$

The ASBC are more general, and they do not depend on the geometry. Theoretically, the surface with the strips can be of any shape, and the strips can be nonperiodical provided that the distance between strips is small enough. For φ-directed strips the ASBC are

$$E_\phi^+ = 0, \qquad E_\phi^- = 0, \tag{5a}$$

$$E_z^+ = E_z^-, \qquad H_\phi^+ = H_\phi^- . \tag{5b}$$

Fig. 5 shows the calculated scattered field from the dielectric cylinder loaded with periodic circumferential strips. The results are obtained by the MoM (accurate results), and by the ASBC and the BCHM methods. The radius and the relative permittivity of the cylinder are $\rho = 1.2$ cm and $\varepsilon_r = 2.1$. The frequency is 10 GHz, and the periodicity and the width of the strips are $P = 0.8$ cm and $W = 0.3$ cm, i.e.0.27 λ_0 and 0.1 λ_0, respectively. The incident wave is TM_z polarized, and angle of incidence is $\theta^{inc} = 90^0$ (normal

incidence). The shown scattered field is normalized to $E_i\sqrt{2j/\pi k\rho}\exp(-jk\rho)$. Both ASBC and BCHM results show a good agreement with MoM results. However, the BCHM method is more accurate and practically there is no difference between MoM and BCHM results. Notice that the radius of curvature is quite small in this example, i.e.

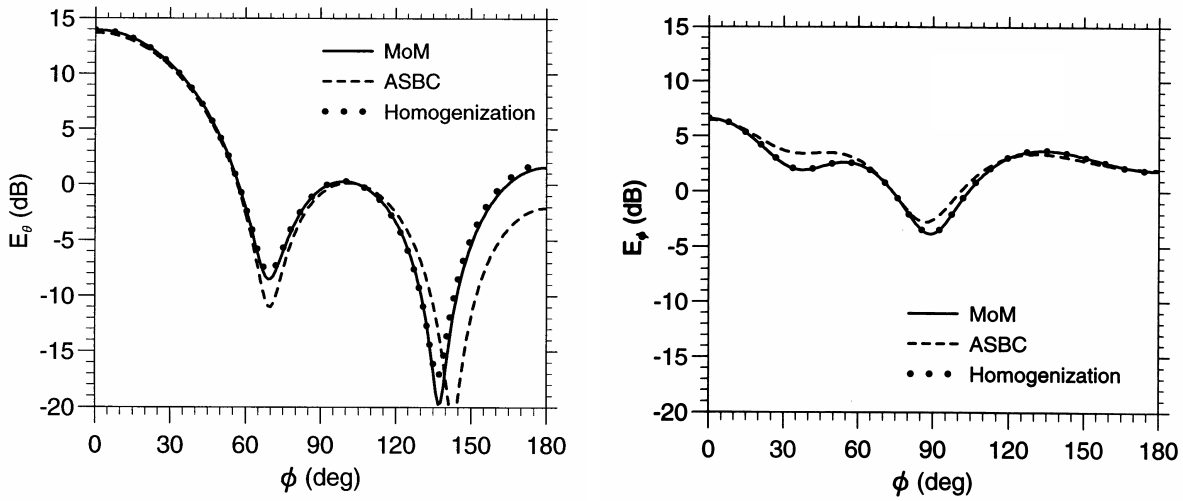

the local planar approximation works well even if the geometry is quite different from the equivalent planar one.

Figure 5. Scattered field from a dielectric cylinder loaded with periodic circumferential strips. (a) TM_z polarized incident wave, (b) TE_z polarized incident wave.

Fig 6. and 7 shows the equivalent blockage width of the scatterer from the previous example. The equivalent blockage is a complex parameter showing how wide the cylinder appears for electromagnetic waves, and it is obtained from the forward scattered field [7]. The incident wave is TE_z polarized in Fig 6 (TM_z polarized in Fig. 7), and the results for two incident angles are shown: $\theta = 60^0$ and $\theta = 90^0$. The numerical results are also compared to the measurements. The results again show that both the ASBC and the BCHM are accurate approximations, and that the BCHM method is more accurate (as in Fig. 2, there is no difference between MoM and BCHM results). It is interesting to mention that although the cylinder has a relatively small radius (0.42 λ_0 at 10 GHz) the local planar approximation used in the BCHM method works very well.

In Fig.6 we have discontinuities in the curves, which are seen in the measured results as well as in the results calculated with the MoM, and which the ASBC can not predict. Like in the planar case the discontinuities are due to the guided modes of the strip-loaded dielectric cylinder. These guided modes correspond to the modes in a conventional metal-walled dielectric-filled circular waveguide that have pure z-directed or φ-directed currents depending on the strip direction, i.e., modes for which the tangential H-field component is orthogonal to the strips. Of symmetry reasons, there are more such modes present for normal incidence. This can also be seen to actually be the case by comparing Fig. 6.a (oblique incidence with $\theta^{inc} = 60^{0)}$ and Fig. 6.b (normal incidence: $\theta^{inc} = 90^0$). The resonance-like phenomena is in Fig. 6.a due to the TE_{01} mode, in Fig. 6.b due to the TE_{21}, TE_{01} and TE_{31} modes.

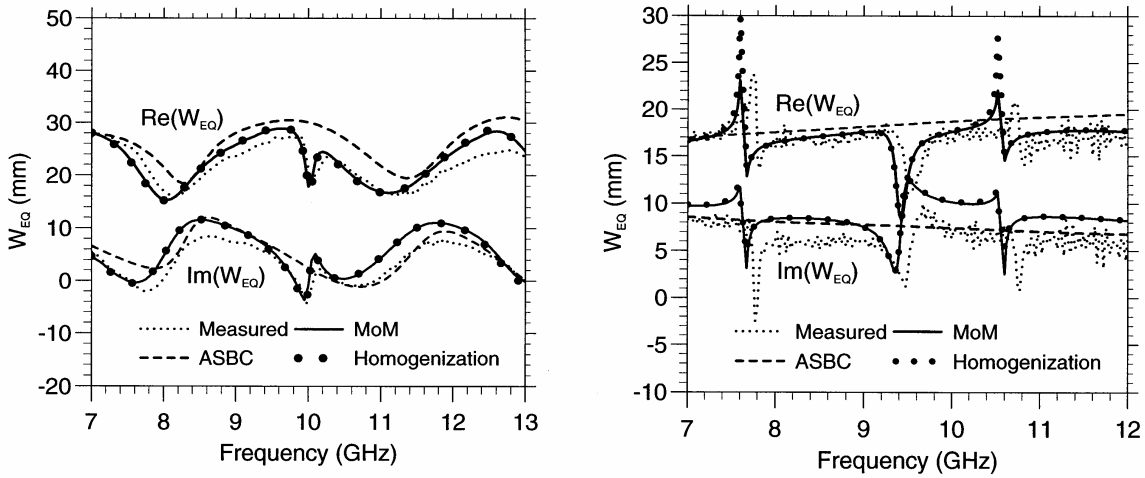

Figure 6. The equivalent blockage width of a dielectric cylinder loaded with periodic circumferential strips for TE_z incident wave. (a) $\theta = 60^0$,(b) $\theta = 90^0$.

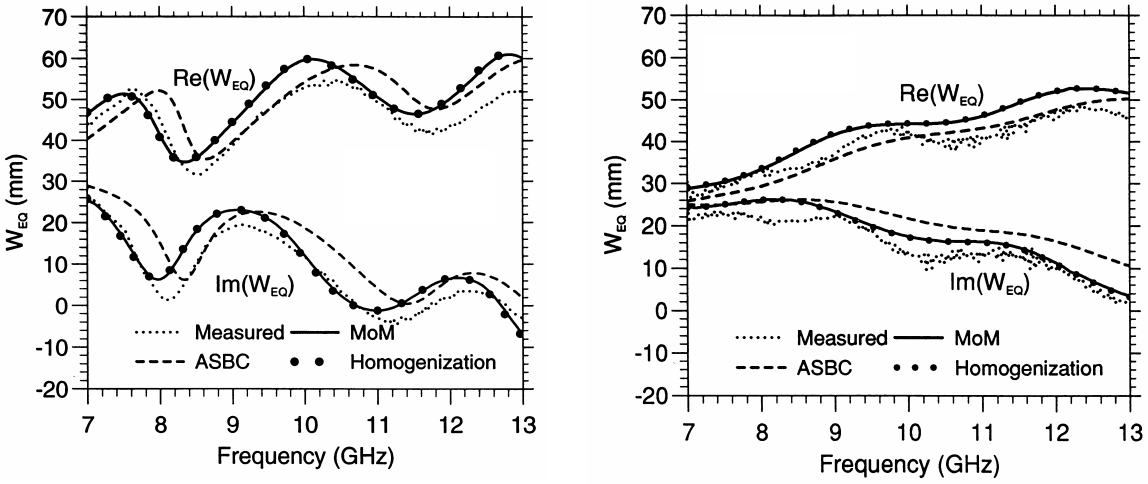

Figure 7. The equivalent blockage width of a dielectric cylinder loaded with periodic circumferential strips for TM_z incident wave. (a) $\theta = 60^0$,(b) $\theta = 90^0$.

References:

[1] Z. Sipus, S. Raffaelli, and P.-S. Kildal, "Periodic strips on planar and circular cylindrical substrates: exact and asymptotic analysis, "*Microwave Opt. Technol. Lett.*, Vol. 17, pp. 173-178, Feb 1998.

[2] A. A. Kishk and P-S. Kildal, "Asymptotic boundary conditions for strip-loaded scatters applied to cylinders under oblique incidence," *IEEE Trans. Antennas Propagat.*, Vol. 45, pp. 51-56, Jan. 1997.

[3] P.-S. Kildal, A. A. Kishk, and Z. Sipus, "Asymptotic boundary conditions for strip-loaded and corrugated surfaces, "*Microwave Opt. Technol. Lett.*, Vol. 14, pp. 99-101, Feb 1997.

[4] F. C. Karal and S. N. Karp, "Propagation of electromagnetic waves along unidirectional screens," in *Electromagnetics Waves*, E. C. Jordan, Pergamon, New York, pp. 967-980, 1963.

[5] F. H. Bellamine, E. F. Kuester, "Guided waves along a metal grating on the surface of a grounded dielectric slab," *IEEE Trans. Microwave Theory Tech.*, Vol. 42, pp. 1190-1197, July 1994.

[6] P-S. Kildal, "Definition of artificially soft and hard surfaces for electromagnetic waves," *Electron. Lett.,* Vol. 24, pp. 168-170, Feb. 1988.

[7] P.-S. Kildal, A. A. Kishk, and Z. Sipus, "Reduction of forward scattering from cylindrical objects using hard struts," *IEEE Trans. Antennas Propagat.*, Vol. 44, pp. 1509-1520, Nov. 1996.

3.1 Range of validity of canonical homogenized problems

Background

Homogenization is a technique which is usually employed when studying problems where the applied wavelength is much larger than the microstructure. The idea is to replace a heterogeneous structure built up of small details with a fictitious, homogeneous structure, which would produce the same scattering characteristics. Strictly speaking, this can only be done in the limit where the wavelength is infinitely large compared to the microscopic details, but in real engineering problems the homogenization procedure still produces acceptable results for finite wavelengths. However, it is usually very difficult to deduce the range of validity for the homogenized results. Some mathematical results, mostly for scalar equations, can be found in [2-7].

In this contribution we treat two separate questions:

1) Under which circumstances is it possible to model a particular structure as a material? For most structures, say a PBG, there is in general an infinite number of degrees of freedom for the electromagnetic field, corresponding to the number of modal solutions. By choosing the frequency low enough, the number of modes can be reduced to only correspond to the possible polarizations of the electromagnetic field.

2) Once the structure is modeled as a material, we may ask how strong the dependence on the scale difference between the wavelength and the microscopic structure is. This corresponds

to identifying the spatial dispersion, which is given by the dependence of the effective permittivity on ka, where k is the wavenumber of the applied field, and a is the typical size of the microstructure.

The first question is addressed in [9, 10, 1], where it is shown that it is possible to define a mathematically rigorous homogenization procedure even in the case when the applied wavelength is finite compared to the microstructure. In fact, it is *necessary* to be able to treat finite scales, since otherwise our models would not be able to describe important effects such as chirality. The typical way of building chiral materials is by including small metallic coils in a matrix material; the coils provide a coupling between the electric field and the magnetic field, but the coupling vanishes for very large wavelengths. The second question is addressed in [8, 11], which investigates spatial dispersion in some specific geometries.

In this contribution, we treat both general results directly from the mathematics, which provides results for any microscopic geometry, as well as a closer look at layered media consisting of two phases. In the latter case, an exact dispersion relation can be found which provides the means for deriving explicit expressions for the homogenized medium.

Ideas behind the mathematical results

The general idea is to define the fictitious, homogenized material as the material which has the same characteristics for wave propagation inside the material. This corresponds to defining the homogenized material from the original structure's dispersion relation and the associated eigenwaves, that is, the typical propagating waves inside the structure. In general, this requires the homogenized material to depend on the wave vector $\mathbf{k}$, that is, we need to include spatial dispersion in the model. The dependence on $\mathbf{k}$ vanishes for small wave numbers, that is, long wavelengths.

This basic idea is simple, but the real trouble consists in proving that it actually provides something *useful*, that is, that the homogenized problem is sufficiently close to the original one. This can be done in a setting where Maxwell's equations can be associated with a compact operator. Compact operators can be identified with infinite-dimensional matrices, which allows for a singular value decomposition, much in the same way as for finite-dimensional matrices. When solving matrix problems with the singular value decomposition, the problem is often regularized by throwing away the smallest singular values, corresponding to using the

Moore-Penrose pseudoinverse. In the case of Maxwell's equations, it can be shown that when the microscopic scale becomes very small, only six singular values can be expected to contribute to make a sizable contribution to the total field. These six degrees of freedom correspond to the six possibilities of choosing polarizations of the electric and the magnetic fields.

The typical setting is to study periodic materials, where the calculcations can be restricted to a unit cell with periodic boundary conditions after applying a Floquet-Bloch transformation of the fields. This transformation requires the typical field to have the representation

$$\mathbf{E}(\mathbf{x}) = e^{i\mathbf{k}\cdot\mathbf{x}}\tilde{\mathbf{E}}(\mathbf{x})$$

where the Bloch amplitude $\tilde{\mathbf{E}}(\mathbf{x})$ is a periodic function of $\mathbf{x}$, and the Bloch wave vector $\mathbf{k}$ is restricted to the first Brillouin zone. The only real change necessary in the equations is to alter the derivatives according to $\nabla \to \nabla + i\mathbf{k}$ and applying periodic boundary conditions. The homogenized material parameters can then be expressed in terms of mean values of the Bloch amplitudes and/or the dispersion relation $\omega(\mathbf{k})$. For more details and explicit representation formulas we refer to [9, 10].

General results for arbitrary geometries

The available mathematical proofs that it is possible to define homogenized materials, albeit using spatial dispersion, requires the following condition to hold (for nonmagnetic materials, the straightforward generalization to bianisotropic media is given in [9, 10]):

$$k_0 a < \frac{\pi - 1}{\|\epsilon(\mathbf{x}) - 1\| + 1} \tag{1}$$

where the supremum norm is used for the complex relative permittivity. The wavenumber $k_0 = \omega/c_0 = 2\pi/\lambda_0$ is the wavenumber pertaining to vacuum, and a is the size of the unit cell. The importance of this condition is that the wavelength does not have to be infinitely larger than the microscopic scale. This is necessary in order to be able to study materials consisting of more or less resonant inclusions, where the dynamics of the electromagnetic field must be accounted for also on the microscopic scale.

This result shows that high contrast media may require large difference in vacuum wavelength λ_0 and cell size a, that is, small $k_0 a$. Note carefully though that (1) is only a sufficient condition for homogenization to be valid, for specific geometries the ho-

mogenized materials may still provide useful results even when this condition is violated.

Spatial dispersion for special geometries

A different kind of question arises when we ask how prominent the spatial dispersion is. This corresponds to estimating the dependence of the effective permittivity on **k**. In [11], the authors investigated the error made if the homogenization was based on infinite wavelength compared to using a finite wavelength for a few specific geometries. The geometries were as depicted below:

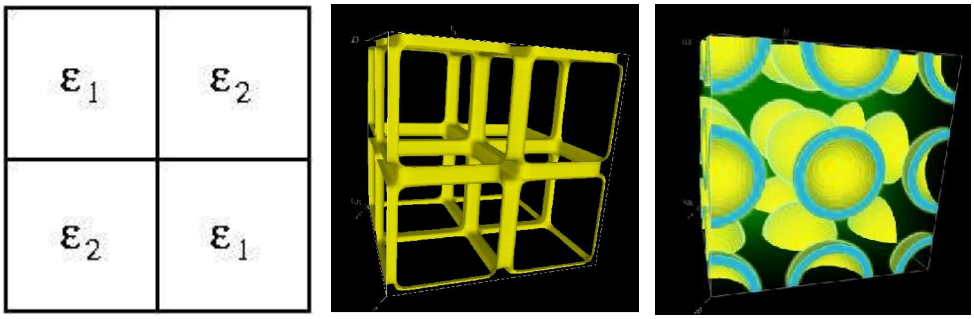

Figure 1: Three canonical geometries. Leftmost is a 2D-geometry, and the scaffold structure and the spherical inclusions on the right are 3D geometries.

The results, as depicted in Figures 2 and 3, indicate that the relative error, defined as

$$\frac{|\epsilon_{\text{eff}}(0)-\epsilon_{\text{eff}}(\mathrm{k})|}{\epsilon_{\text{eff}}(\mathrm{k})}$$

did not exceed 10% if the contrast was less than 10. The effective permittivity $\epsilon_{\text{eff}}(0)$ corresponds to the effective permittivity calculated using infinite wavelength, and $\epsilon_{\text{eff}}(\mathrm{k})$ is the effective permittivity calculated using a finite wavelength.

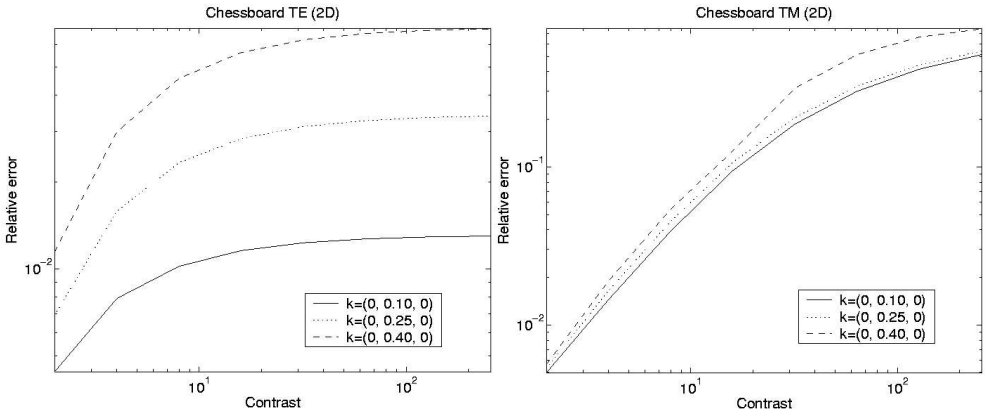

Figure 2: Results for the 2D chessboard geometry.

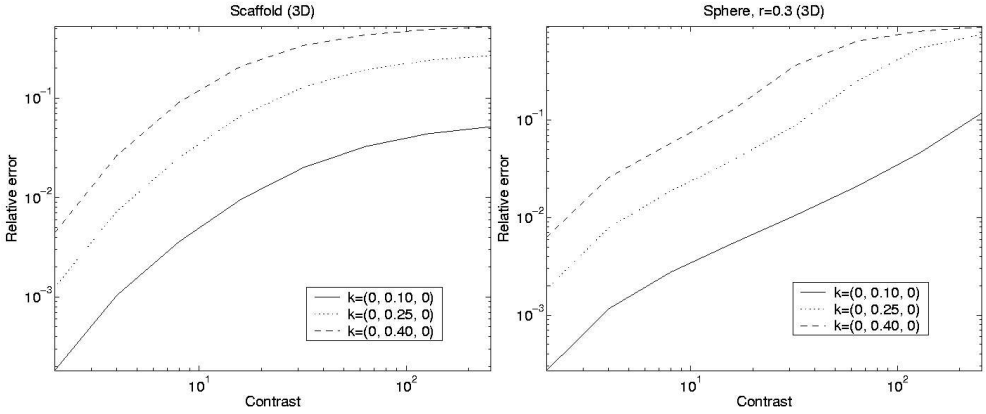

Figure 3: Results for the 3D scaffold and spherical geometries.

For layered media with two phases ϵ_1 and ϵ_2, each occupying a volume fraction of f_1 and f_2 and layered in the z direction, the following asymptotic expressions for the effective permittivity can be obtained [1]:

$$\epsilon_{\text{eff}}^{\text{p}} = f_1\epsilon_1 + f_2\epsilon_2 + \frac{1}{12}\frac{(\epsilon_1-\epsilon_2)^2(f_1 f_2)^2}{f_1\epsilon_1 + f_2\epsilon_2}(ka)^2 + O((ka)^4)$$

for polarizations parallel to the material interfaces, and

$$\epsilon_{\text{eff}}^{q}(\mathbf{k})=\left[\left(\frac{f_1}{\epsilon_1}+\frac{f_2}{\epsilon_2}\right)\sin^2\theta+\frac{1}{f_1\epsilon_1+f_2\epsilon_2}\cos^2\theta\right]^{-1}$$

$$+\frac{1}{12}\frac{(\epsilon_1-\epsilon_2)^2(f_1f_2)^2}{f_1\epsilon_1+f_2\epsilon_2}\left(\frac{(f_1\epsilon_1+f_2\epsilon_2)^2}{\epsilon_1\epsilon_2}\sin^2\theta-\cos^2\theta\right)^2(ka)^2$$

$$+O\left((k_0a)^4\right)$$

for polarizations in the plane spanned by the wave vector **k** and the normal to the material interfaces (the z direction), with the angle θ being the angle between the wave vector and the z direction. From these expressions it is evident that the spatial dispersion, that is, the dependence of the effective permittivity on **k**, is proportional to $(\epsilon_1-\epsilon_2)^2(f_1f_2)^2$ for small wave numbers. This shows that the spatial dispersion is more important for composite materials with high contrast and sizable volume fractions, than for almost homogeneous materials with low contrast.

Another interesting observation is that by choosing the propagation angle according to

$$\theta=\arctan\frac{\sqrt{\epsilon_1\epsilon_2}}{f_1\epsilon_1+f_2\epsilon_2}$$

the spatial dispersion can be minimized for one of the polarizations. However, since the permittivity is minimal in this direction, the material will act as a concave lense and spread out a ray packet centered around this direction. Once again, specific geometries may be more robust against spatial dispersion than others.

Conclusions

A heterogeneous structure may be modeled as a homogeneous material, even if the applied wavelength is not infinitely large compared to the microscopic scale. We have presented a sufficient condition for arbitrary geometries, but a wider range of validity for specific geometries can be anticipated.

Spatial dispersion is expected to be more important for composite materials with high contrast and sizable volume fractions, than for almost homogeneous materials with low contrast.

References

[1] G. Allaire, Y. Capdeboscq, A. Piatnitski, V. Siess, and M. Vanninathan. Homogenization of periodic systems with large potentials. Arch. Rational Mech. Anal., 174, 179–220, 2004. doi:10.1007/s00205-004-0332-7.

[2] C. Conca, R. Orive,and M. Vanninathan. Bloch approximation in homogenization and applications. SIAM J.Math.Anal., 33, 1166-1198, 2002.

[3] S. S. Ganesh and M. Vanninathan. Bloch wave homogenization of scalar elliptic operators. Asymptot.Anal., 39, 15-44, 2004.

[4] R. C. Morgan and I. Babuska. An approach for constructing families of homogenized equations for periodic media. I: An integral representation and its consequences. SIAM J.Math. Anal., 22, 1-15, 1991.

[5] R. C. Morgan and I. Babuska. An approach for constructing families of homogenized equations for periodic media. II: Properties of the kernel. SIAM J.Math.Anal., 22, 16-33, 1991.

[6] F. Santosa and W. W. Symes. A dispersive effective medium for wave propagation in periodic composites. SIAM J.Appl.Math., 51, 984-1005, 1991.

[7] E.V.Sevostyanova. Asymptotic expansion of the solution of a second-order elliptic equation with periodic rapidly oscillating coefficients, Mat.Sb.(N.S.),115, pp.204-222, 1981 (in Russian); Math.USSR-Sb., 43, pp.181-198, 1982 (in English).

[8] D. Sjöberg. Exact and asymptotic dispersion relations for homogenization of stratified media with two phases. Submitted to Journal of Electromagnetic Waves and Applications. Preprint available at www.es.lth.se.

[9] D. Sjöberg. Homogenization of dispersive material parameters for Maxwell's equations using a singular value decomposition. Multiscale Model. Simul., 4(3), 760-789, 2005. doi:10.1137/040614153

[10] D. Sjöberg, C. Engström, G. Kristensson, D. J. N. Wall, and N. Wellander. A Floquet-Bloch decomposition of Maxwell's equations, applied to homogenization. Multiscale Model. Simul., 4(1), 149-171, 2005. doi:10.1137/040607034

[11] D. Sjöberg, G. Kristensson, and C. Engström. Validity of homogenization using Bloch waves. In International Conference on Electromagnetics in Advanced Applications (ICEAA), Torino, Italy, pages 455-458. September 8-12 2003.

3.2 Effects of manufacturing tolerances

This contribution consists mainly of results from a Master's Thesis written by Lovisa Nord at Lund University, who studied the influence of manufacturing tolerances on wave propagation in frequency selective radomes. This work was supported by the Swedish Defence Materiel Administration, and was motivated by a need from the radome industry to get a better understanding of the impact of various design parameters. We refer to [3] for the full report, which is publicly available, and give only a brief summary with some representative results here.

The manufacturing of a radome

This section provides a rough description of the radome manufacturing process as performed at Chelton Applied Composites AB in Linköping, Sweden.

The radome is constructed on a metal tool. This serves as a mould, and should thus have the same shape as the intended radome. Nose cone radomes are for instance made on a tool shaped as a cone.

Monolithic radomes, i.e., radomes consisting of only one material, are mostly made from a composite. This material is created during the manufacture of the radome, and is a mixture of glass fiber weave and some kind of plastic, for instance polyester. The permittivities of the two components are different, and mixing them in the correct proportion gives the composite its specified effective permittivity. Pieces of the woven material are adhered to the manufacturing tool, with thin layers of the liquid polyester in between. A vacuum pump is used to pump out any air left between the layers, in order to prevent bubbles or gaps of air. When the radome has the correct thickness it is dried and tempered with the help of ultraviolet radiation, after which a cutter cuts it to its specified outer shape. The radome's electrical thickness is then tested by measuring the insertion phase delay (IPD) of every part of the radome. This can be adjusted by modifying the local thickness.

Stratified radomes are manufactured similarly, but here the layers of different materials must also be glued together, usually with an epoxy glue. If composites are used they are created on the tool as described above, but foam materials are glued to the other layers in thicker pre-made slabs.

Any FSSs used are usually etched on a dielectric substrate covered with metal film, the same kind of process that is utilized for making printed circuits. The FSSs are then adhered to the other parts of the radome on the manufacturing tool.

Manufacturing defects

There is a multitude of errors that can be made in the manufacturing of a radome. There will always be slight deviations from the intended design, as the manufacturing precision is only finitely accurate. The properties of the materials used may also vary.

Defects in the dielectric layers may concern thickness, permittivity or conductivity. In a purely dielectric radome the electrical properties are controlled by those parameters only.

The permittivity of a dielectric is usually specified only as a permittivity interval. Deviations from an exact value are thus common. Small thickness variations are probably rather frequent as well, caused directly or indirectly by the manufacturing process or mechanical wear. High-speed flights through rain may for example erode the radome so that its outer walls gradually become thinner. Also, the conductivity (or imaginary part of the complex permittivity, representing the bulk losses) may deviate from the specified values.

Another scenario for errors is that the wanted materials are not available. A good theoretical radome design may exist where the parameters are chosen to yield the desired properties. The manufacturing “error” may then only be that the wished for materials are not available so that materials of slightly different permittivity or thickness must be used instead.

When considering the FSSs involved, numerous defects may appear, of which many concern the elements. For instance the shape of the elements may be slightly wrong and this could concern just one element, some elements, or all of them, depending on the source of the error. The same applies to the size and placing of the elements. They might erroneously be placed non-periodically or non-symmetrically. However, as is shown in [4], the effect on the far field pattern is negligible if the error is much smaller than the wavelength. The manufacturing process for the FSS as such is very reliable, and thus we do not consider errors in this layer. However, effects arising from the difficulties of applying a double-periodic FSS on a doubly curved radome may still appear.

If the radome contains two FSSs, it is probable that those are not placed exactly opposite to each other, i.e., there may be an offset between them. If the radome is doubly curved, as most radomes must be to enclose an antenna, an offset between the two FSSs is inevitable if the two surfaces are separated some distance from each other. The curvature then makes them experience slightly different curve radii. This case is investigated in [2], where it is suggested that the distance between the FSSs may need to be as large as three quarters of a wavelength for this effect to be safely neglected.

Errors may also occur during the assemblage of the radome layers. Due to the doubly curved shape, the layers can easily become uneven, and air gaps or air bubbles may appear. Unevenness should be unavoidable, since when planar sheets are glued to the doubly curved surface, some areas must become thicker than others. This may also cause the local permittivity to vary.

Furthermore, the radome can be poorly constructed so that it does not bear the heat and mechanical wear that it might be exposed to when in use, and air cracks can then develop after some time of usage. This is more probable if the radome contains one or more FSS. The metal and the dielectrics have very different thermal expansion coefficients, so at the high temperatures that can develop during flight, caused by friction, different layers of the radome might expand differently. If the construction is weak, this may result in an air crack between those layers [1].

Test radome

To investigate the effects of manufacturing tolerances, an example radome from [1] was chosen and is depicted below.

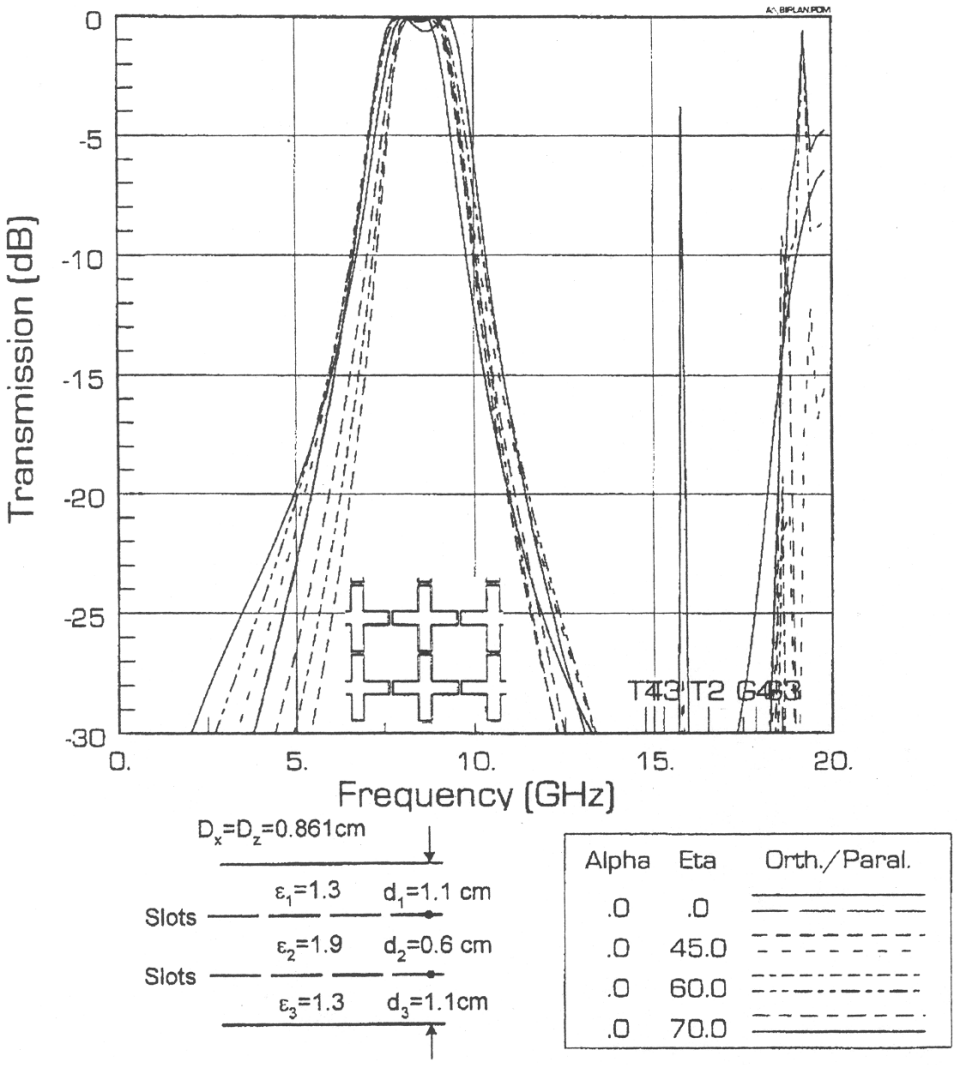

Figure 1: Transmission properties of a hybrid radome from [1, p. 248].

The hybrid radome consists of two FSS sheets, separated by a dielectric and surrounded by two additional dielectric slabs. The behavior of this radome was investigated using the program developed by Widenberg in [5]. Since some of the dimensions of the geometry are not given in [1], some initial work was done to find a geometry which approximately produces the same transmission data as in Figure 1.

Not all of the possible manufacturing errors listed in the previous section were investigated. The following selection of parameters were studied in [3]:

- Inclusion of glue layers in the model, with variations in thickness and permittivity.
- Inclusion of air gaps in the model, with variations in location.
- Losses in the inmost dielectric.
- Variations in total thickness of the radome, varying both in the inner and the outer dielectric layers.
- Optimum design compared to using commercially available materials.

In this text, we only report on some representative results, i.e., the inclusion of glue layers, the influence of losses in glue layers close to the FSS, variations in thickness of the radome, and the impact of using off-the-shelf materials instead of design values.

Results

As noted above, not all the results from the simulations are reported here, and we refer to the full report [3] for more details. In particular, the full report demonstrates simulations with more angles of incidence.

The inclusion of glue layers in the model is most critical near the FSS. This can be interpreted in terms of the FSS as a resonant structure, depending strongly on the wavelength employed. Since the wavelength is theoretically scaled by the square root of the permittivity, a glue layer with strong contrast compared to the bulk dielectric sheets may substantially change the resonance frequency of the FSS. This is shown by the figures below.

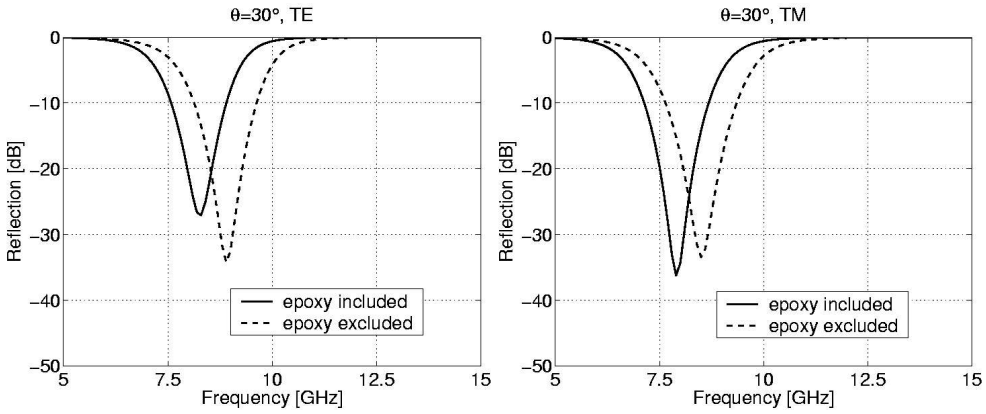

Figure 2: Reflection from a radome model including epoxy layers compared to reflection from a radome model that excludes them.

Losses in the glue layer do not seem to be that critical. To get a noticeable effect, the losses had to be made one or two orders larger in magnitude than the commercially available glue, as demonstrated in Figure 3.

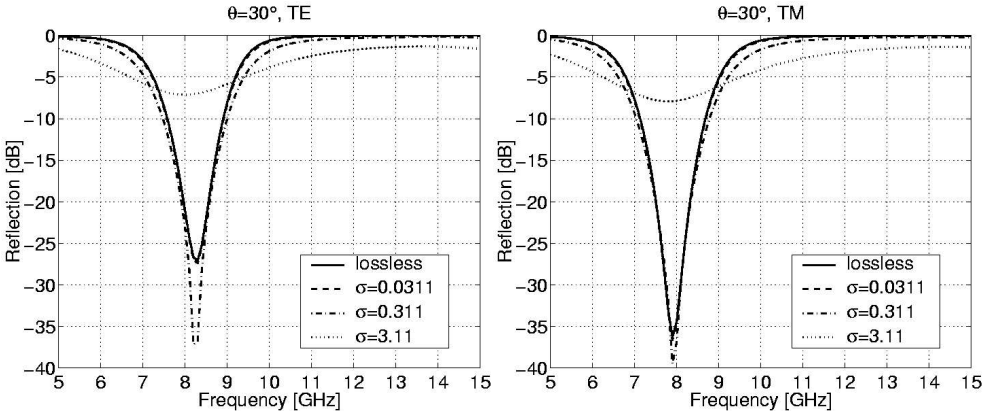

Figure 3: Effects of losses in a glue layer adjacent to the FSS. The conductivity values are given in S/m, and the lowest value correspond to realistic values for the glue used in production.

When changing the thickness of the dielectric layers of the radome, the electrical properties are much more sensitive to changes in the layer separating the two FSSs, as shown in Figure 4. This can be interpreted by noting that the region between the FSSs can be seen as a cavity, and a change in the thickness changes the resonance frequency of that cavity, whereas a change in thickness of the outmost dielectric layers mostly influence the angular bandwidth of the radome.

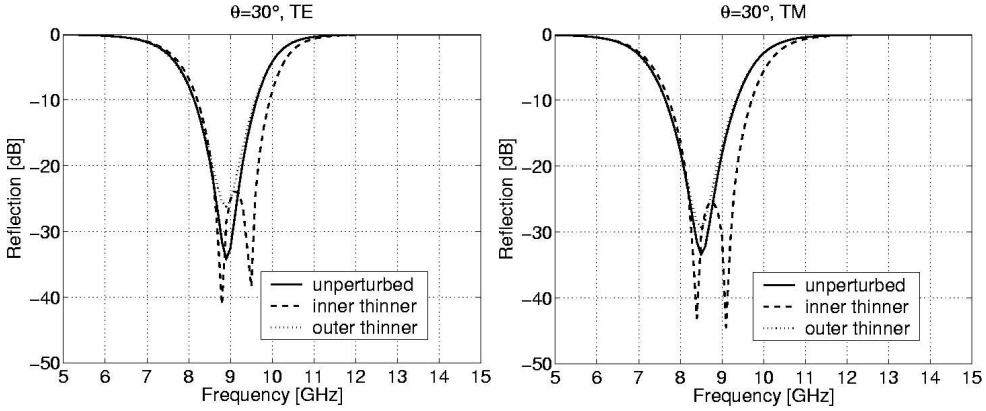

Figure 4: Reflection from the unperturbed Munk radome is compared to the reflection from a radome that is 1 mm thinner. The dashed line represents a 1 mm thickness decrease in the inner radome layer, and the dotted line represents a thickness decrease of 0.5 mm in each of the outer layers.

To conclude this section, we discuss the result of using off-the-shelf materials when realizing a design. At the radome production plant, only a restricted range of dielectric materials are available. In Figure 5, the materials closest to the desired design parameters are given together with simulation data.

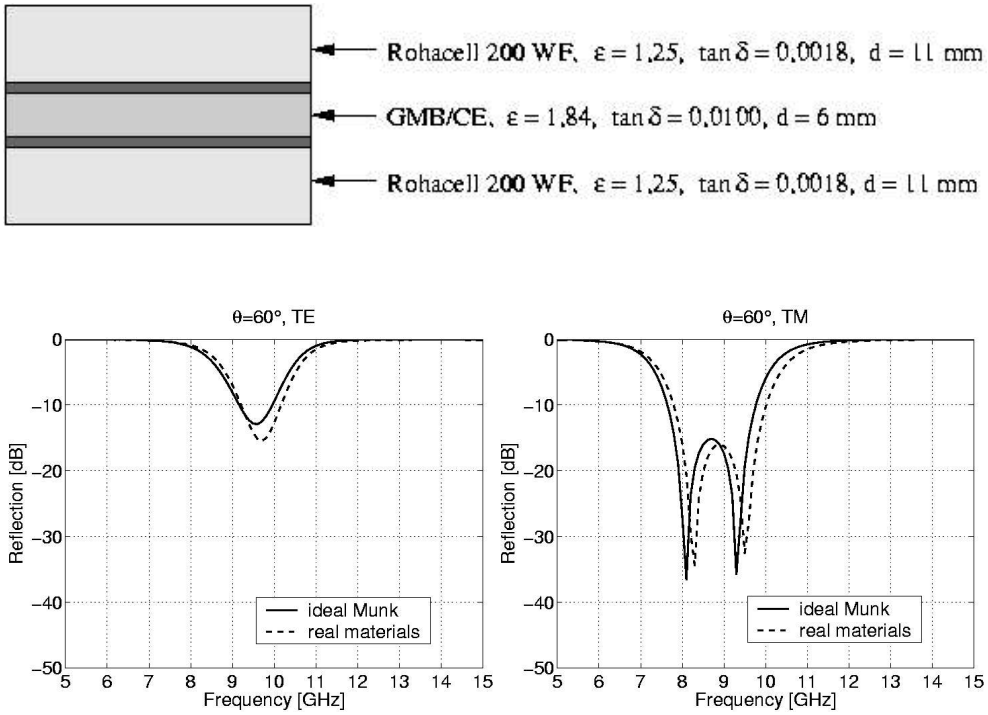

Figure 5: Reflection of Munk's optimally designed radome compared to that with commercially available materials.

Conclusions

We have given some examples of the effects of manufacturing tolerances on wave propagation characteristics of frequency selective radomes. One important common feature evolves from these results, namely that it is important to be thorough and use tight tolerances on geometries which constitute a resonant structure. Furthermore, small losses, either in thin glue layers or in bulk dielectrics, do not seem to be very important when studying reflection data. It is more pronounced in transmission data, as shown in [5].

Even if small changes in thickness of nonresonant parts of the structure do not influence the reflectance of the radome much, it may influence the phase of the transmitted field to such a degree that a pointing error appears, i.e., the antenna behind the radome is not radiating in the desired direction. At present, this is checked by tedious measurements and manual fixes by the radome manufacturer, which might be eliminated if the antenna is “trained” to compensate for the radome. This is possible at least for phased array antennas.

References

[1] B. Munk. Frequency selective surfaces: theory and design. John Wiley & Sons, New York, 2000.

[2] R. Lagerholm and T. Stanek. Effect of layer offsets on dichroic radomes. IEEE Antennas and Propagation Society International Symposium, 3, 2124-2127, 1994.

[3] L. Nord. Sensitivity of wave propagation characteristics to manufacturing defects in frequency selective radomes. Master's thesis, TEAT-5073, Dept. Electroscience, Lund Institute of Technology, P.O. Box 118, 221 00 Lund, Sweden. 2005. www.es.lth.se

[4] D. Sjöberg. Coherent effects in single scattering and random errors in antenna technology. Progress in Electromagnetics Research, 50, 13-39, 2005.

[5] B. Widenberg. Thick frequency selective structures. PhD thesis, Department of Electroscience, Lund Institute of Technology, P.O. Box 118, 221 00 Lund, Sweden, 2003. ISSN 1402-8662.

Test Case
Multi-layer Frequency Selective Surface
Parametric analysis of the effects of manufacturing tolerances

TNO

November 11, 2005

1 Layout

The periodic structure considered for this test case consists of two equal dipole-based Frequency Selective Surfaces (FSS) printed on the two sides of a dielectric slab, made of Taconic TLY 5, a Duroid with dielectric constant 2.2 (FSS core). The FSS geometry is indicated in Fig. 1a. The folded dipoles have dimensions d_w=3.3 mm, d_l=5.1 mm and w=0.3 mm, and are arranged in a triangular grid characterized by d_1=21 mm, d_2=13.83 mm and skew angle $\Omega = 40.6°$. The double FSS is matched to free space by means of two slabs of Bisco Cellular Silicone HT-820 foam, with an average permittivity of 1.64. The supplied foam layers are stuck together with a bonding film having permittivity 2.32. The layout of the structure is shown in Fig. 1b, while the thickness of the various layers is indicated in Tab. 2 and the permittivity of the materials, with corresponding tolerances, is shown in Tab. 1.

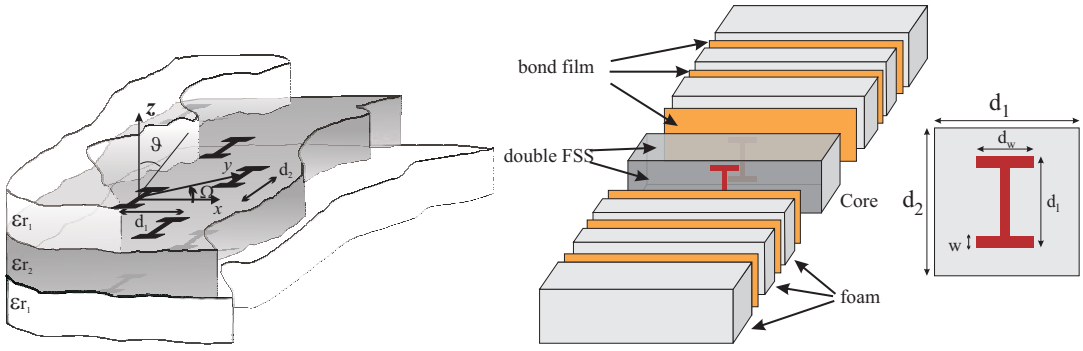

(a) (b)

Figure 1: Multi-layer FSS. (a) FSS geometry (the bonding film is not shown in this figure). (b) Final structure of the manufactured FSS.

Dielectric	Permittivity and tolerance
Foam (Bisco HT-820)	1.64 ± 0.12
Bonding film (Arlon 6250)	2.32 ± 0.10
Fiberglass/PTFE (Taconic TLY5)	2.2 ± 0.02

Table 1: Permittivity of the dielectric slabs in the manufactured FSS panel.

Layer	Thickness (mm)
Foam	3.1
Bonding film	0.1
Foam	2.2
Bonding film	0.1
Foam	2.2
Bonding film	0.1
copper cladding	0
Fiberglass/PTFE	4.5
copper cladding	0
Bonding film	0.1
Foam	2.4
Bonding film	0.1
Foam	2.4
Bonding film	0.1
Foam	3.1

Table 2: Thickness of the dielectric slabs in the manufactured FSS panel.

2 IEMEN results

The reflection and transmission coefficients of the structure described in the previous section are shown in Fig. 2, for the case of TE plane wave incidence with respect to the plane of incidence $x - z(\phi = 0)$, and for four incidence angles $\vartheta = 0°, 15°, 20°, 25°$. These results have been simulated by means of the Multimode Equivalent Network approach based on the Integral Equation formulation (IEMEN)described in the Catalogue of Software for Reflector Surface Modelling - ACE WP2.3-2 Reflector Surface Models and in the references reported there. Note that the losses of the materials and the ohmic losses of the FSS elements have not been included in these simulations. Moreover, as permittivity we have used the theoretical values indicated in Tab. 1, while the tolerances have been reported to interpret deviations from the measurement results of Sec. 3.

3 Measurements

The transmission measurement setup is shown in Fig. 4. The measured transmission coefficient is shown in Fig. 3.

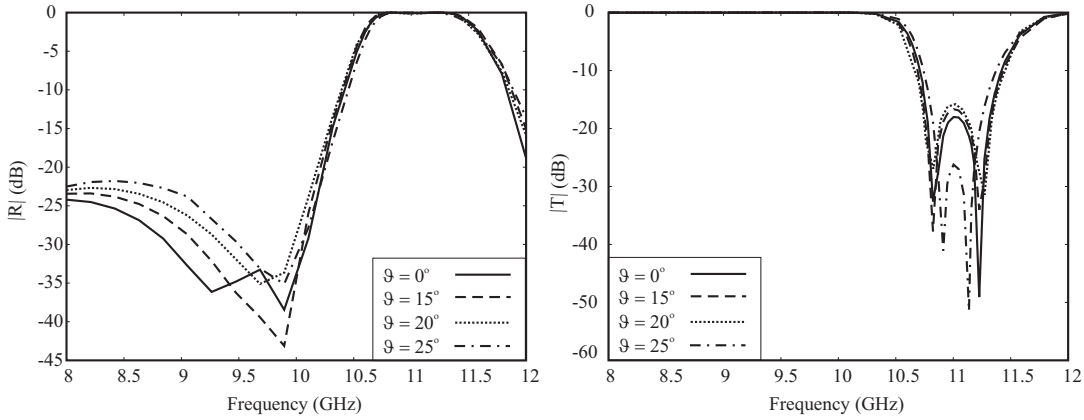

(a) (b)

Figure 2: IEMEN simulation results of the manufactured FSS for the angles of incidence: $\vartheta = 0°$, 15°, 20° and 25°. (a) Amplitude of the reflection coefficient. (b) Amplitude of the transmission coefficient.

4 Parametric study

The Arlon bonding film is optimized for PTFE-based laminates; in this case the typical temperature and pressure needed to flow the adhesive and ensure the bonding are 120^{o}C and 6.4 tons respectively, applied for about 10 minutes. However, while for the bonding of the foam to the Taconic board the FSS manufacturer could stick to these standard values, the foam-to-foam bonding required a higher temperature and pressure. In particular, the FSS panel was vacuum pressed at 20 tons for one hour, at a temperature of 150^{o}C. As a consequence, the bonding process slightly changed the thickness and the dielectric properties of both the foam and the bonding film in a non-predictable way.

To assess the FSS sensitivity to the dielectric profile (dielectric constant, tangent loss and thickness of each dielectric slab) and other geometrical dimensions, a parametric study has been performed on the FSS performances as a function of the following parameters:

- dielectric constant of the bonding film;
- dielectric constant of the foam;
- thickness of the bonding film;
- thickness of the foam;
- dipole dimensions;
- alignment of the two arrays;
- dielectric losses.

In all cases, we have considered broadside plane wave incidence with polarization on the H plane.

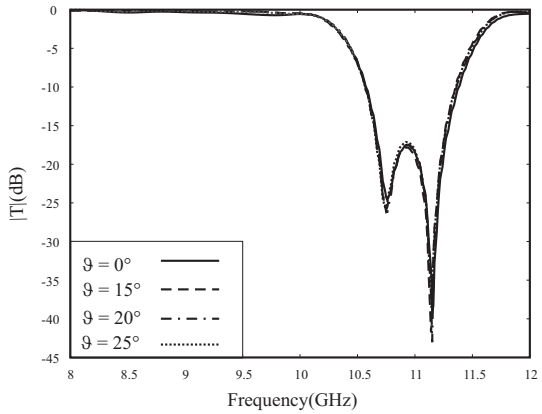

Figure 3: Amplitude of the transmission coefficient measured for different incidence angles, using the setup shown in Fig. 4.

Dielectric constant of the bonding film The nominal value of the dielectric constant of the Arlon bonding film is 2.32. However, because of difficulties encountered in bonding the foam with the FSS core (Duroid), an additional adhesive was used to improve the adhesion. Since the dielectric properties of the adhesive were not indicated by the manufacturer, coaxial probe measurements of permittivity were performed at TNO on samples of Arlon bonding film + adhesive extracted from the panel. Values as high as 3 were observed.

In view of this, we have compared the performances of the FSS structure for three values of the bonding film permittivity: 1.6, 2.3, 3. As shown in Fig. 5, a change in the permittivity of about $\pm$ 25% corresponds to a shift of the resonance frequency of $\pm$ 2.5%.

Dielectric constant of the foam The external FSS layer was made of Bisco Cellular Silicone HT-820, an high-performance silicone foam produced by Rogers Corporation. This foam consists of a spongy core covered by a smooth uniform surface, with a nominal permittivity of 1.5 at 60 Hz. Tests were performed to determine the dielectric properties of the foam in the operating X-band. The range of possible permittivity values predicted by Rogers Corp. was 1.52-1.76, with a medium value of 1.64. A similar value was measured at TNO by means of the coaxial probe test instrument. Note that, since the material is not homogeneous, only an average dielectric constant can be considered. Furthermore, the temperature and pressure needed for bonding could have slightly changed the dielectric properties of the material. In view of this, it is important to evaluate the effect of a change in the foam permittivity on the FSS performances.

The FSS structure has been simulated for three values of the foam permittivity: 1.52, 1.64, 1.76. Fig. 6 show that a change of the permittivity of the 12% introduces a shift of the resonance frequency of the structure of $\pm$1.0%.

Thickness of the bonding film The nominal thickness of the bonding film is 0.0381mm. However, because of problems encountered when bonding the foam layer with the Duroid, several layers of different bonding films were overlapped. In Fig. 7 we have compared the FSS performances for three values of the bonding film thickness: 0.1mm $\pm$ 0.05mm. As can be seen, although these layers are more than one order of magnitude smaller than the other

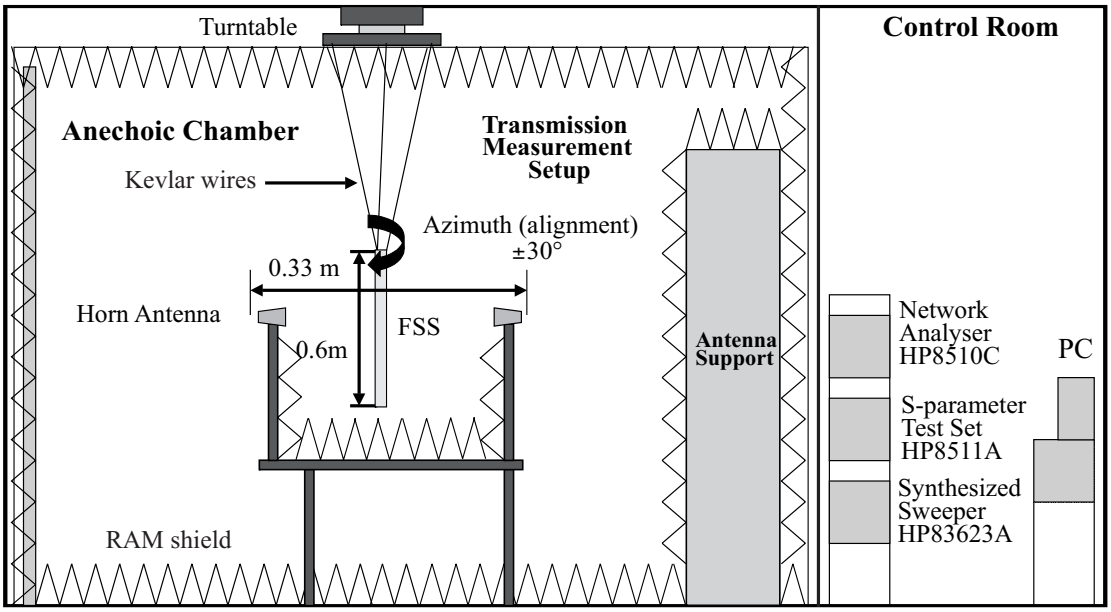

Figure 4: Schematic of the transmission measurement setup

dielectric layers, still they have a significant impact on the FSS performances.

Thickness of the external foam layer The nominal thickness of each foam slab, as indicated by the manufacturer, was 2.54mm. However, the actual value of this thickness, measured by our workshop in the delivered structure, was 3.1mm for the external slabs and between 2.2mm and 2.4mm for the four internal layers. Also this effect could be explained by the stress applied to the foam in the bonding phase. We have considered here the effect of a deviation of ± 0.6mm on the total thickness (8%), which corresponds to ± 0.2mm on each layer's thickness. Results are shown in Fig. 8. No significant deviations have been observed in the -3dB stop band. This result could be expected since the dielectric permittivity of the foam layers was relatively close to one (air).

Length of the dipoles Some differences between the dimensions of the dipoles indicated in the design and those in the actually manufactured structure were observed. These manufacturing errors were not systematic, in the sense that not all of the elements were effected by the same error. In general, it is too complicate to characterize the effect of random errors. In this case, in fact, the structure should have been considered non-periodic and it would have been necessary to apply a full-wave analysis with an element-by-element approach. Such an approach is not feasible, or at least is extremely heavy from the computational point of view, because of the very large number of elements. Nevertheless, in order to have an idea of the impact of these differences, simulations were performed assuming a uniform deviation applied to all the elements. This, of course, can be considered the worst case, since all the elements contribute coherently to the error. Simulations were performed for different lengths of the dipole vertical and horizontal arms (length of the dipole vertical arm equal to 5mm, 5.1mm and 5.2mm and length of the horizontal arms equal to 3mm, 3.3mm and 3.6mm). The width

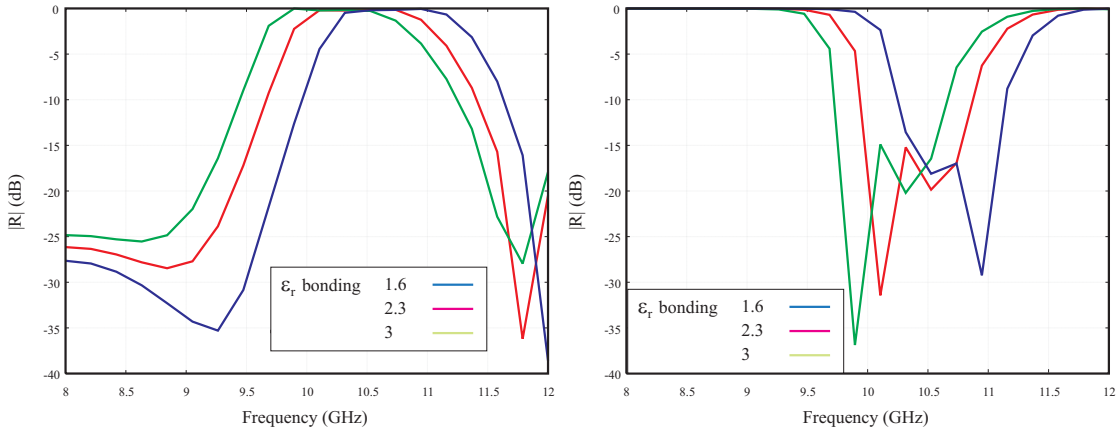

(a) (b)

Figure 5: Effect of the permittivity of the bonding film. (a) Reflection coefficient. (b) Transmission coefficient.

was also changed from 0.28mm to 0.3mm and 0.32mm. These variation were based on the average errors observed on the printed elements. Fig. 9 and Fig. 10 show the effect of a change in the length of the vertical and of the horizontal arm of the dipole, respectively. The performances of the FSS after a change in the dipole width of $\pm$ 0.02mm are shown in Fig. 11.

Alignment of the two arrays In the design, the two FSS's have to be perfectly aligned. We have evaluated the effect of a misalignment between the elements of the two arrays, by introducing a shift of 0.1mm along the x-direction and along the y-direction. Fig. 12 show the corresponding reflection and transmission coefficient. As could be expected, the effect of the shift in the horizontal dimension is the only one having a significant impact. This is basically due to the fact that the shift in the x-direction determines a larger decoupling of the elements with respect to the corresponding case of shift in the y-direction. In this last case, in fact, the effect is only a little (in percentage) sliding along the main dimension.

Effect of the losses in the dielectric Furthermore, we have evaluated the effect of the losses in the dielectric layers on the performances of the FSS structure. In particular, we have included in the simulations the tangent loss of the Duroid, as indicated by Taconic in the data sheet: 0.0009, and the one of the foam as measured by Rogers: 0.0981. The tangent loss of the Arlon bonding film is 0.0013, but, since information about the losses of the other adhesive was not made available by the manufacturer and could not be recovered by measurements with the coaxial probe, the losses associated to the bonding process were not included in this analysis. Fig. 13 shows the reflection coefficient of the structure where the losses were included compared with that of a structure made of perfect dielectric. The insertion loss, as difference between the maximum reflection coefficient with and without losses, is about 0.54 dB, as can be observed in the detail of the curves in the figure inset.

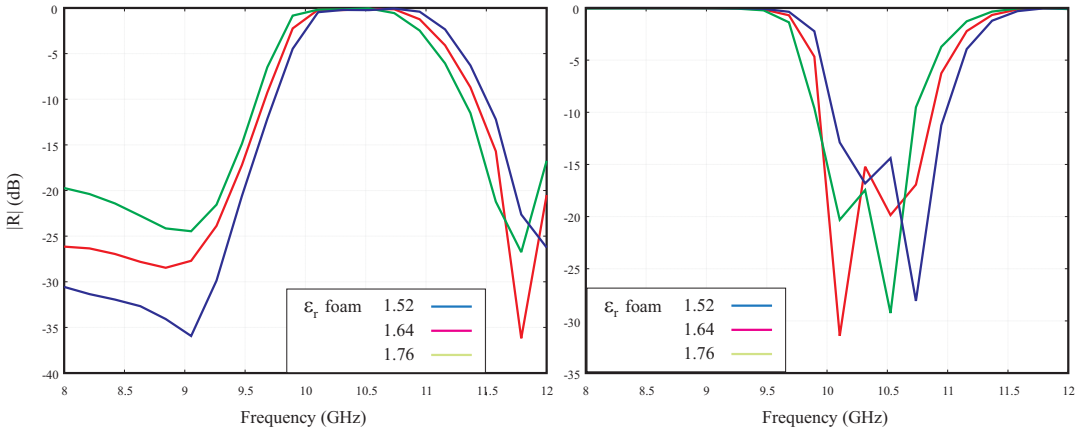

(a) (b)

Figure 6: Effect of the foam permittivity. (a) Reflection coefficient. (b) Transmission coefficient.

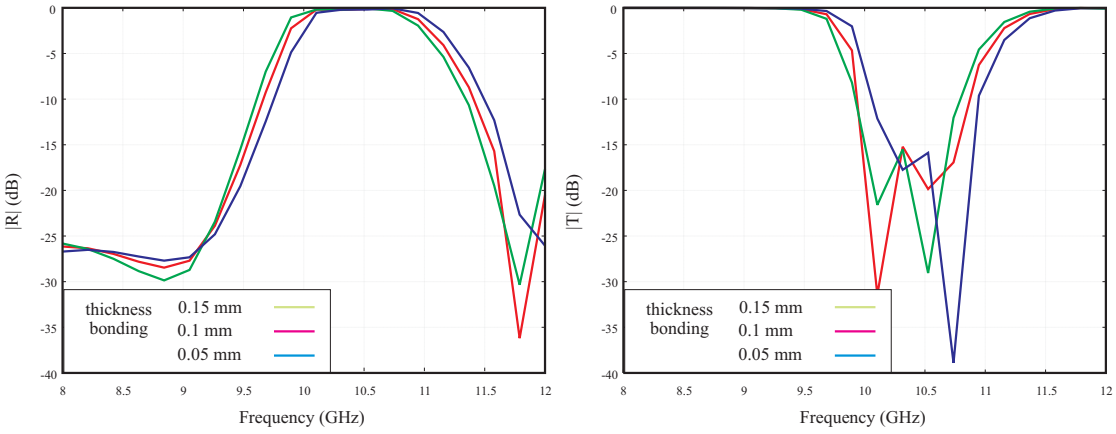

(a) (b)

Figure 7: Effect of a change in the thickness of the bonding film.(a) Reflection coefficient. (b)Transmission coefficient.

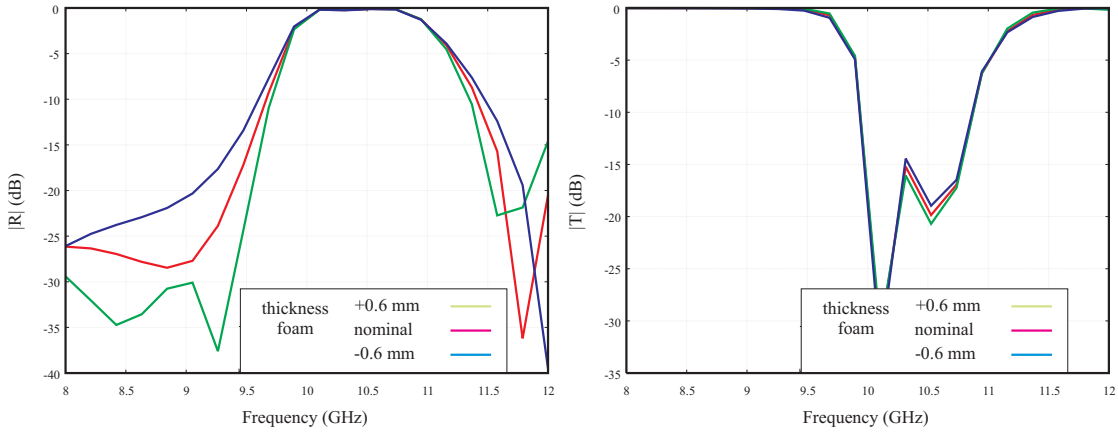

(a) (b)

Figure 8: Effect of a change in the thickness of the foam. (a) Reflection coefficient. (b) Transmission coefficient.

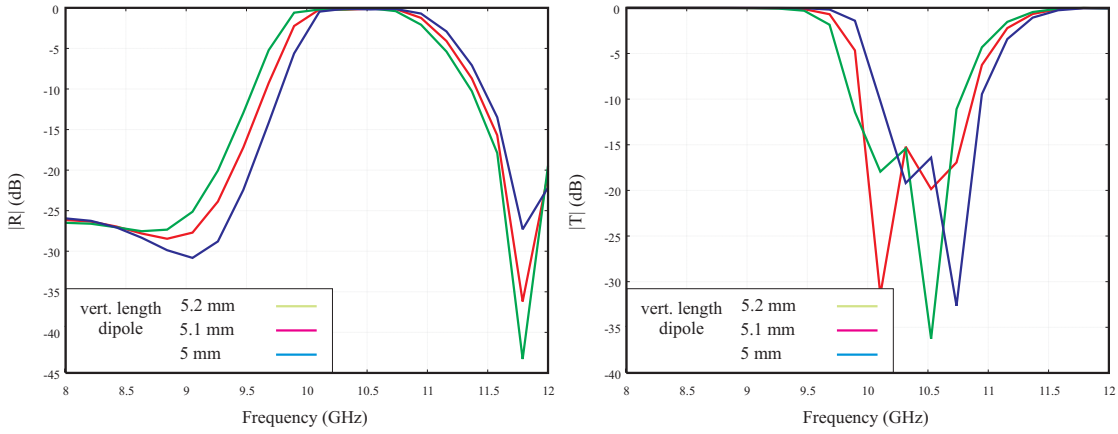

(a) (b)

Figure 9: Effect of a change in the length of the vertical arm of the dipole. (a) Reflection coefficient. (b) Transmission coefficient.

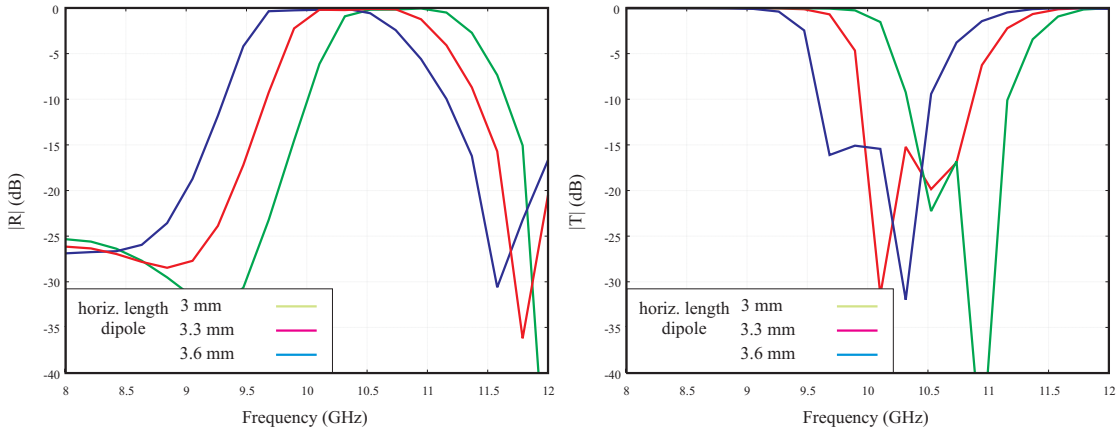

(a) (b)

Figure 10: Effect of a change in the length of the horizontal arm of the dipole. (a) Reflection coefficient. (b) Transmission coefficient.

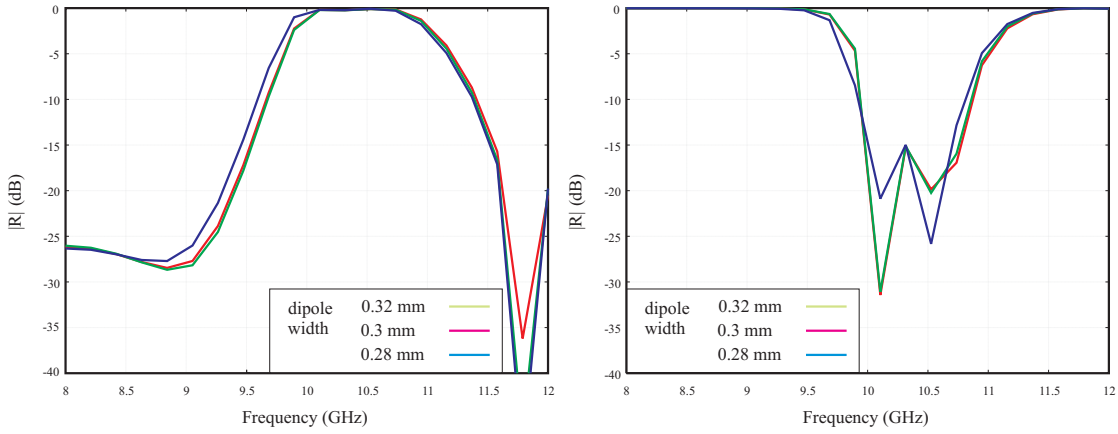

(a) (b)

Figure 11: Effect of a change in the dipole width. (a) Reflection coefficient. (b) Transmission coefficient.

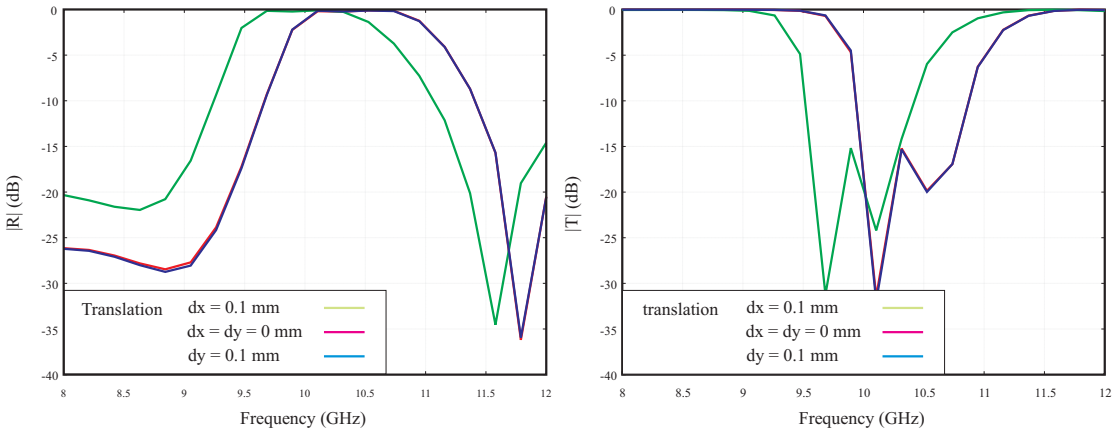

(a) (b)

Figure 12: Effect of a misalignment of the two arrays in the x- and in the y-direction. (a) Reflection coefficient. (b)Transmission coefficient.

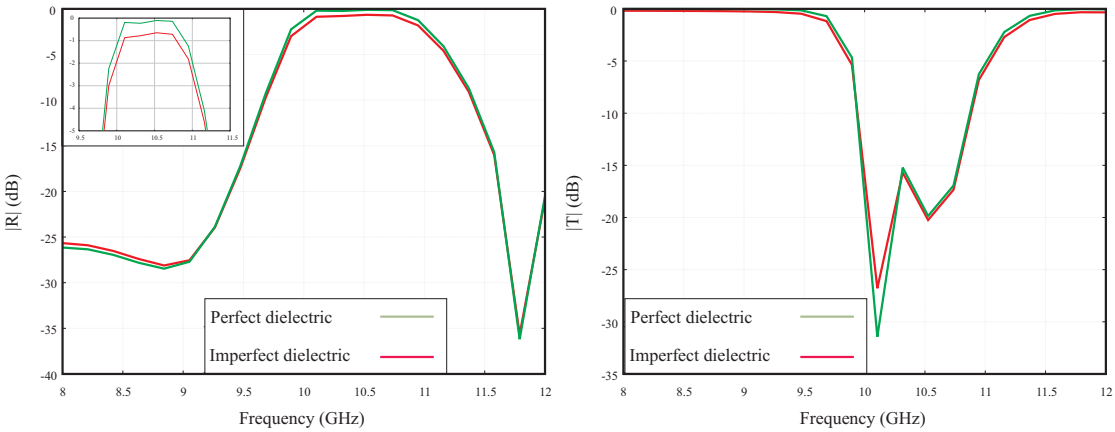

(a) (b)

Figure 13: Effect of the losses in the dielectric slabs on the performances of the FSS in Fig. 1b. (a) Reflection coefficient. (b) Transmission coefficient

5. Effects from manufacturing tolerances

In this section an example of sensibility to patch manufacturing tolerances will be shown.

We consider a capacitive FSS made up of vertical dipoles arranged on a rectangular lattice, with geometry described in the following Figure 4.3a:

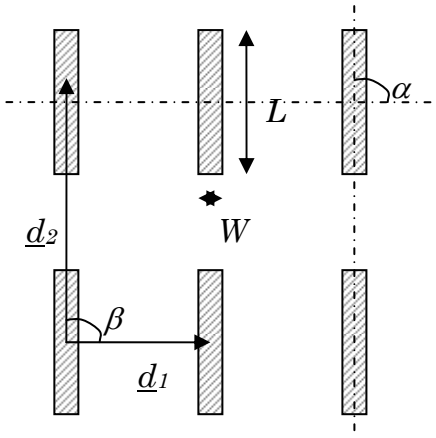

Figure 4.3a. Geometry of the capacitive FSS

The actual dimension are: L = 15 mm, W = 1.5 mm, d1 = 12 mm, d2 = 18 mm. The frequency response of such a device, for normal incidence, is represented in Figure 4.3b

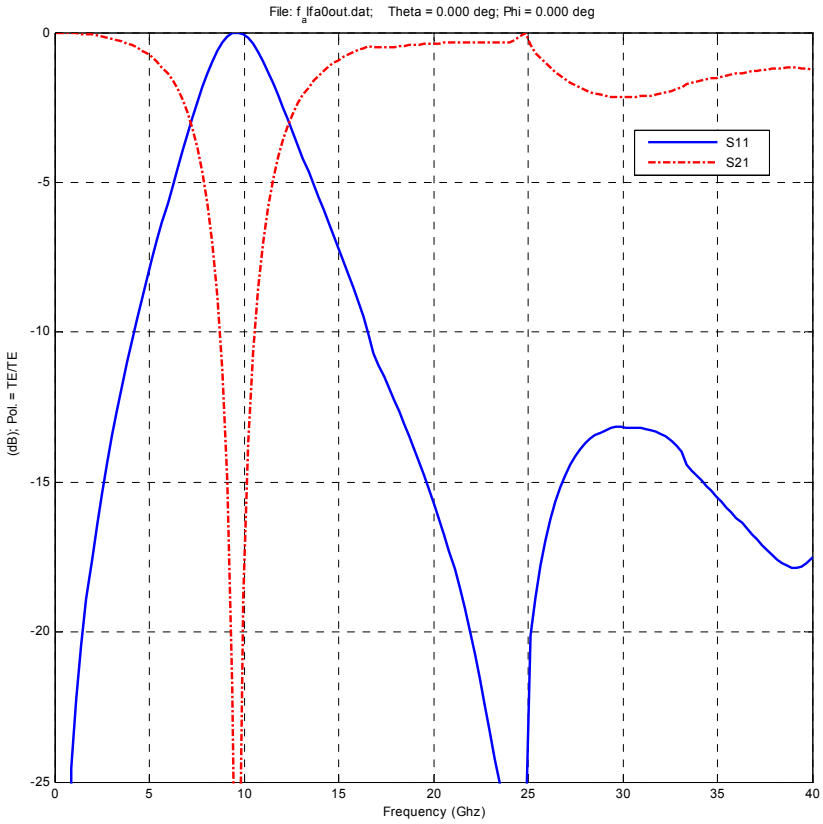

Figure 4.3b. Frequency response of the capacitive FSS (normal incidence)

First of all, let us assume that the FSS was realised with a manufacturing tolerance on the inclination of the patches, which results in a variation of the angle α. To analyse the effect of varying such a parameter, initially a constant rotation was applied to all patches. If all patches were printed with the same inclination, the most relevant effect is a shift in the resonance frequency, which appears to be shifted down about 1.5% for inclination variation of 5 degs.

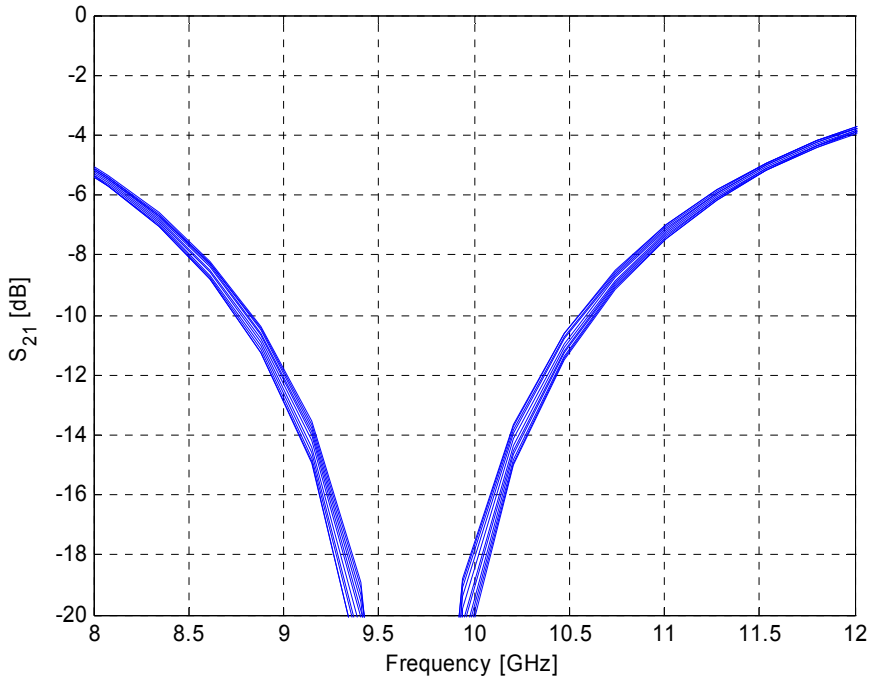

Figure 4.3c. Frequency responses of capacitive FSSs (normal incidence) with α as a parameter, from 0 to 5 degs.

Morevoer, an asymmetrical non-uniform distribution of patches as been investigated. To obtain the result, a parametric study was performed taking into account a random variation of α, with a Gaussian distribution of values between 0 degs and 5 degs. Several simulations were run, changing the average value and the variance of the statiscal distribution. The most relevant effect is that it is sufficient to have 10% of the patches shifted, to degrade the frequency behaviour of the FSS.

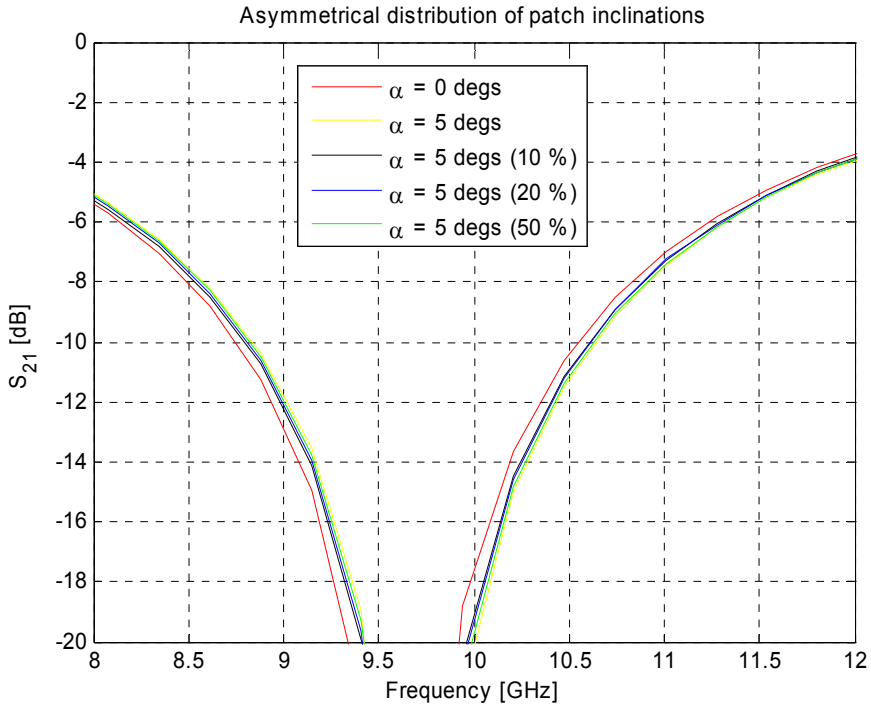

Figure 4.3d. Frequency responses of capacitive FSSs (normal incidence) with a statistical variation of α as a parameter, between 0 degs and 5 degs.

Finally, a symmetrical non-uniform distribution of patches was investigated. To obtain the result, a parametric study was performed taking into account a random variation of α, with a Gaussian distribution of values between -5 degs and 5 degs. Several simulations were run, changing the average value and the variance of the statiscal distribution. Like the asymmetric case, the most relevant effect is that it is sufficient to have 10% of the patches shifted, to degrade the frequency behaviour of the FSS. Even if the patches distribution appear to macroscopically uniform the shape of the array, the result is downgraded, like the asymmetrical one.

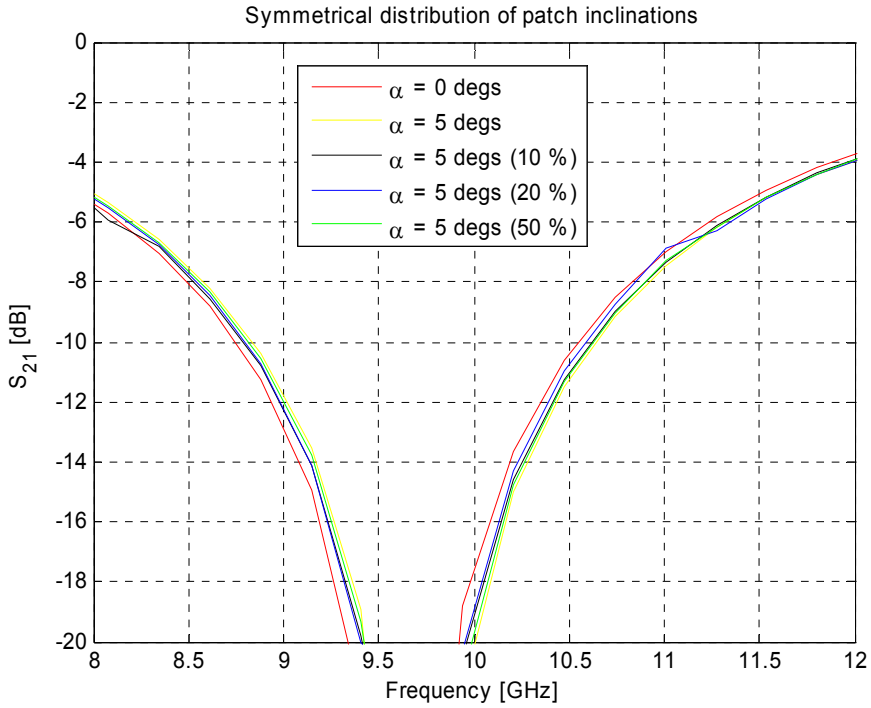

Figure 4.3d. Frequency responses of capacitive FSSs (normal incidence) with a statistical variation of α as a parameter, between -5 degs and 5 degs.

6. Fast approximate methods compared to rigorous solutions

For the investigation of reflector antennas with surfaces other than perfectly conducting it is essential that fast and reliable software is available to model the local reflection and transmission properties everywhere on the surface. It is the purpose of the present chapter to illustrate the validity of approximate methods for strip grids and rectangular meshes by comparing them to accurate Method of Moments solutions.

The rigorous and the approximate methods are described in Sections 6.1.1 and 6.1.2, respectively and the comparisons between them are presented in Sections 6.2 and 6.3 for strip grids and rectangular meshes, respectively.

6.1 Solution methods

6.1.1 Rigorous solution

Politecnico di Torino has developed the computer program "METallic STrIps Simulator (MESTIS)" and the associated manual (Orta et al., 2001). The program is based on a Method of Moments approach and it is possible to model one or more layers of co-planar strip grids and each layer can consist of one, two or three strip grids making arbitrary angles with each other. A layer with three strip grids is illustrated in Figure 6-1. In addition, it is possible to model dielectric layers around and between the different strip grids.

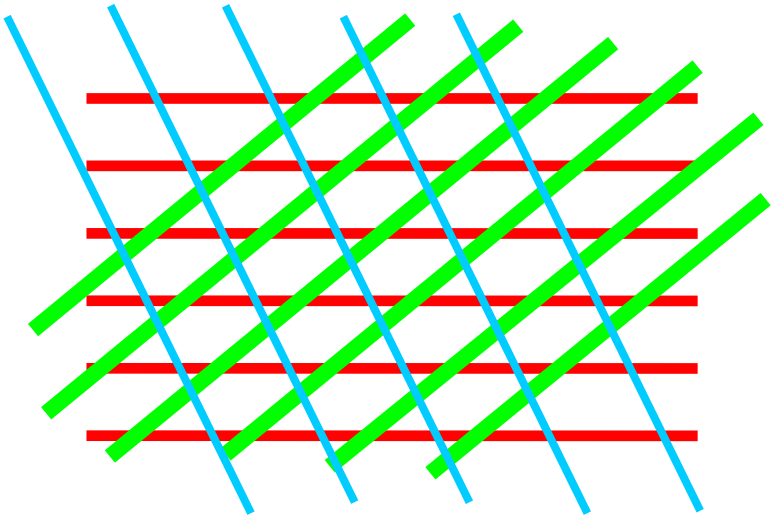

Figure 6-1 Example of three co-planar strip grids forming a two-dimensional periodic structure

The electromagnetic properties are in MESTIS described by the so-called scattering matrices. In order to be able to use the results in the reflector antenna program, GRASP9, it is necessary to transform the scattering matrix parameters into the reflection and transmission coefficients required by GRASP9 (Pontoppidan, 2005).

The main driver for the development of MESTIS was to be able to analyse the electrical properties for two or more co-planar non-parallel strip grids in electrical contact. Therefore only the current component along the strip is included whereas the component orthogonal to the strip is neglected since it will be very small compared to the currents flowing in the other set of strips.

Also another software package for strip grids from Torino is available, ASG (Analysis of Strip Gratings). This package deals with only one or two parallel strip grids, but here also the current components orthogonal to the strip direction are taken into account.

The two software packages mentioned above will be used to evaluate the faster but more approximate methods implemented in GRASP9.

6.1.2 Approximate methods

A planar sample of a general reflector material is illustrated in Figure 6-2. The direction of an incident plane wave is given by the spherical coordinates (θ_i, ϕ_i), where θ_i is measured from the posi-

tive z-axis and ϕ_i from the positive x-axis. The angle θ_i is limited to the range $0° \leq \theta_i < 90^o$.

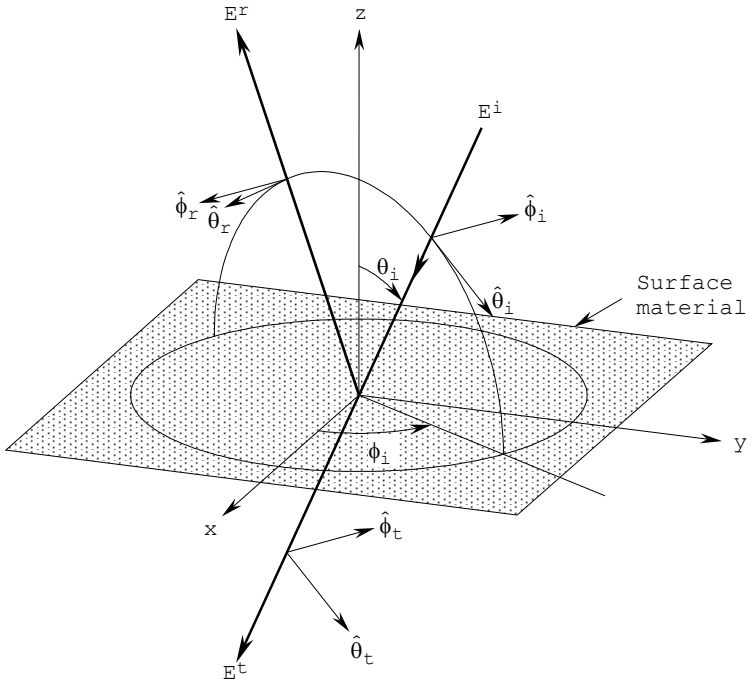

Figure 6-2 Unit vectors for the definition of reflection and transmission coefficients in GRASP9.

The incident plane wave can be decomposed as

$$\bar{E}^i = E^i_\theta \hat{\theta}_i + E^i_\phi \hat{\phi}_i \tag{6-1}$$

and is partly reflected and partly transmitted through the surface. The unit vectors of incidence, $\hat{\theta}_i$ and $\hat{\phi}_i$, are the usual polar vectors shown in Figure 6-2.

The reflected field is given by

$$\bar{E}^r = E^r_\theta \hat{\theta}_r + E^r_\phi \hat{\phi}_r \quad , \tag{6-2}$$

where

$$\begin{Bmatrix} E^r_\theta \\ E^r_\phi \end{Bmatrix} = \begin{bmatrix} R_{\theta\theta} & R_{\theta\phi} \\ R_{\phi\theta} & R_{\phi\phi} \end{bmatrix} \begin{Bmatrix} E^i_\theta \\ E^i_\phi \end{Bmatrix} \tag{6-3}$$

and the unit vectors of reflection, $\hat{\theta}_r$ and $\hat{\phi}_r$ are the negative mirror images of $\hat{\theta}_i$ and $\hat{\phi}_i$, respectively. Similar relations can be set up for the transmitted field.

6.1.2.1 Strip grid

A strip grid consists of parallel strips. Each strip has a width w and the spacing of the strips is s (the distance from the centre of one strip to the centre of the next).

The reflection and transmission coefficients are given by Nakamura and Ando (1988). For a plane wave at normal incidence, $\theta_i = \phi_i = 0$, polarised parallel to the strips the reflection coefficient is

$$\begin{aligned} R_{\theta\theta} &= \frac{1}{1+jt} \\ t &= -\frac{2s}{\lambda}\ln\left(\cos(\frac{\pi}{2}(1-\frac{w}{s}))\right) \end{aligned} \tag{6-4}$$

and for polarisation orthogonal to the strips one gets

$$\begin{aligned} R_{\phi\phi} &= \frac{jt'}{1+jt'} \\ t' &= -\frac{2s}{\lambda}\ln\left(\sin(\frac{\pi}{2}(1-\frac{w}{s}))\right) \end{aligned} \tag{6-5}$$

where λ is the wavelength. Expressions (6-4) and (6-5) show that if the spacing relative to the wavelength, s/λ, is reduced while the ratio between the width and the spacing, w/s, is kept constant, $R_{\theta\theta} \to 1$ and $R_{\phi\phi} \to 0$.

For incidence angles other than normal the reader is referred to (Nakamura and Ando, 1988).

6.1.2.2 Wire grid

The wire grid material consists of a planar sheet of parallel circular cylindrical wires of spacing s. The diameter of the wires is d_0. It is assumed that $d_0 << s$.

The wire grid has many similarities to the strip grid and it can be shown that for polarisation parallel to the wires the reflection is equal to that of a strip grid where the strip width $w = 2d_0$ (Butler, 1982). The angular dependence with θ_i and ϕ_i is the same as for the strip grid.

6.1.2.3 Rectangular mesh

The rectangular mesh grid consists of two orthogonal sets of wires as illustrated in Figure 6-3. The spacing between the wires is s_x

and s_y for the wires in the x- and y-direction, respectively. The wire diameter is d_0 and the two sets of wires are in electrical contact at all the intersection points.

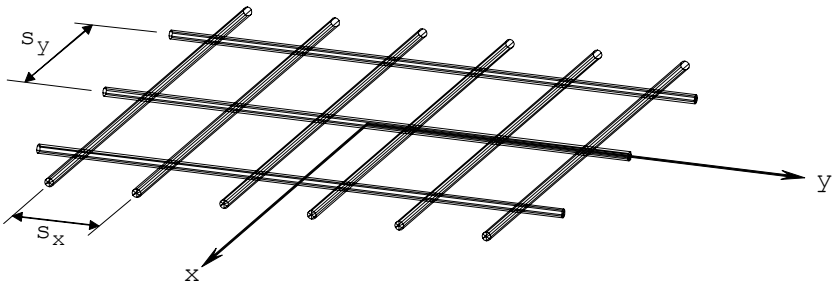

Figure 6-3 Rectangular mesh

The reflection and transmission coefficients used in GRASP9 are based on Astrakhan (1968). For normal incidence in one of the principal planes, for example $\phi_i = 0$, the reflection coefficients are practically identical to those for the wire grid, i.e. $R_{\theta\theta}$ is the same as for the wire grid with spacing s_x.

6.2 Strip grids

This section presents a number of numerical experiments for single strip grids such as strip grids in free space, strip grids immersed in a dielectric and strip grids located on the one side of a dielectric.

For all the examples the reflection and transmission properties are illustrated by just one of the components of the reflection and transmission matrices, namely the magnitude of $R_{\theta\theta}$. The reason for this important simplification is that it has been observed that all the components behave in a similar fashion and it is therefore sufficient to investigate only one of them.

6.2.1 Strip grid in free space

A single strip grid is considered and the strips are parallel to the x-axis in Figure 6-2. The parameters for the strip grid are

frequency = 10 GHz (λ = 30 mm)
strip spacing, s = 1.5 mm
strip width, w = 0.1 mm

The results are shown in Figure 6-4. The left side of the plot shows the amplitude of $R_{\theta\theta}$ calculated by MESTIS as a function of the angle of incidence (θ, ϕ). θ varies from 0º to 60° and ϕ varies from 0º to 90°. The figure shows that the amplitude is maximum in the plane of the strips, $\phi = 0°$, and minimum in the plane orthogonal to the strips, $\phi = 90°$.

The results obtained by GRASP9 for this example are almost identical as identified by the right side of Figure 6-4 which shows the difference between $|R_{\theta\theta}|$ obtained by MESTIS and GRASP9. The maximum difference appears at normal incidence and it is around 0.25 per cent. The same order of agreement exists for the other components of the reflection matrix. The selected strip dimensions are typical for practical applications and the accuracy obtained with GRASP9 is more than acceptable.

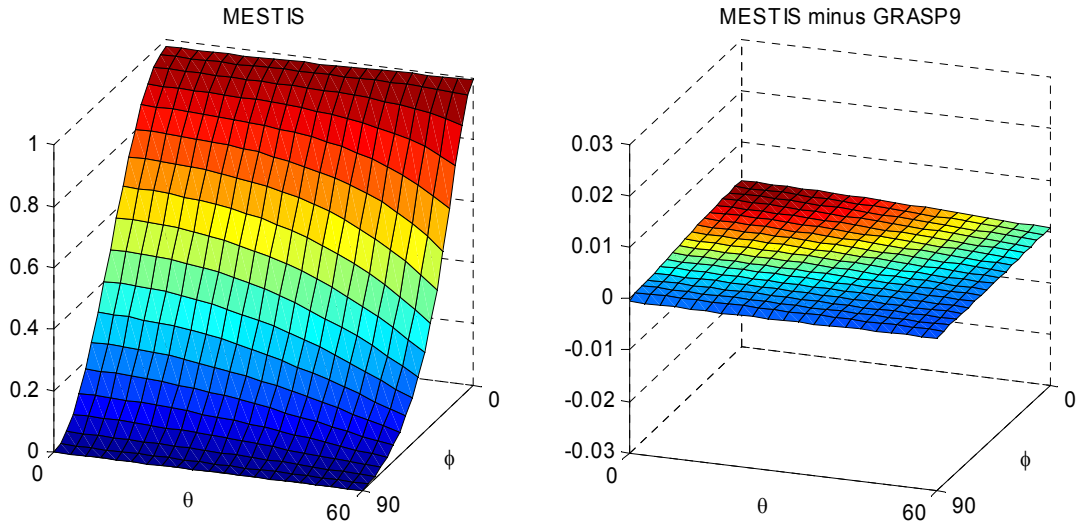

Figure 6-4 Reflection coefficient for single strip grid in free space, $s = 1.5$ mm, $w = 0.1$ mm

In the next example the strip spacing is still 1.5 mm but the width is increased to 0.5 mm or one third of the spacing. The results are shown in Figure 6-5 and it is seen that the accuracy is very good except for ϕ near to 90º. The reason to this is that neglecting the currents orthogonal to the strips is not acceptable for wide strips. The example was therefore also investigated with ASG and the obtained reflection coefficient for normal incidence and ϕ = 90º were:

MESTIS: 0.
GRASP9: 0.0144
ASG: 0.0147

This verifies the orthogonal component as given by (6-5).

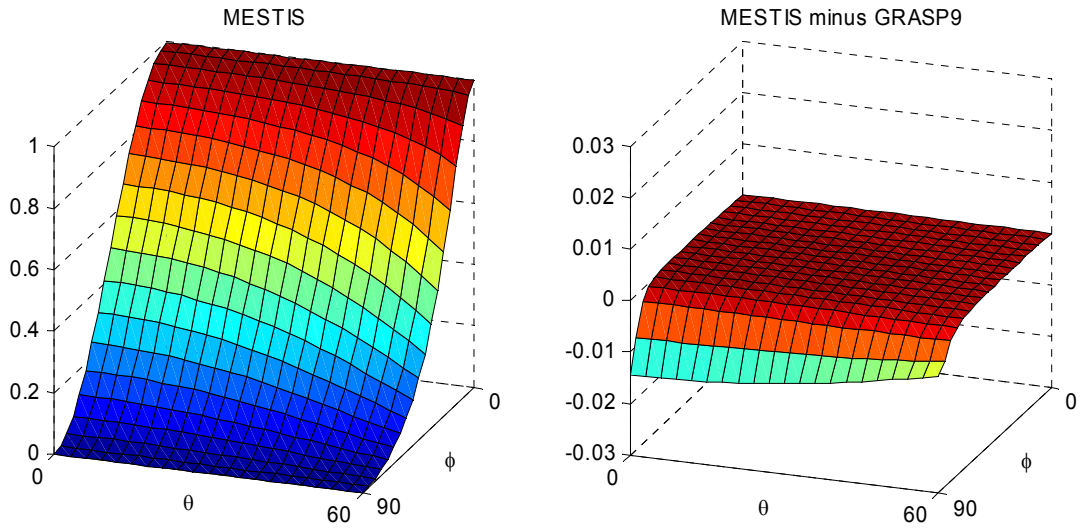

Figure 6-5 Reflection coefficient for single strip grid in free space, $s = 1.5$ mm, $w = 0.5$ mm

In the last example of strip grids in free space the strip width is reduced to 0.01 mm. The result is shown in Figure 6-6. This result is surprising since one would intuitively expect a better agreement when the strip width is reduced. The example was therefore also investigated with ASG and the obtained reflection coefficient for normal incidence and $\phi = 0^o$ were:

MESTIS: 0.9535
GRASP9: 0.9102
ASG: 0.9271

Again there is a good agreement between GRASP9 and ASG and we must conclude that there is probably a problem in MESTIS for very narrow strip widths. For realistic strip widths it seems to work fine.

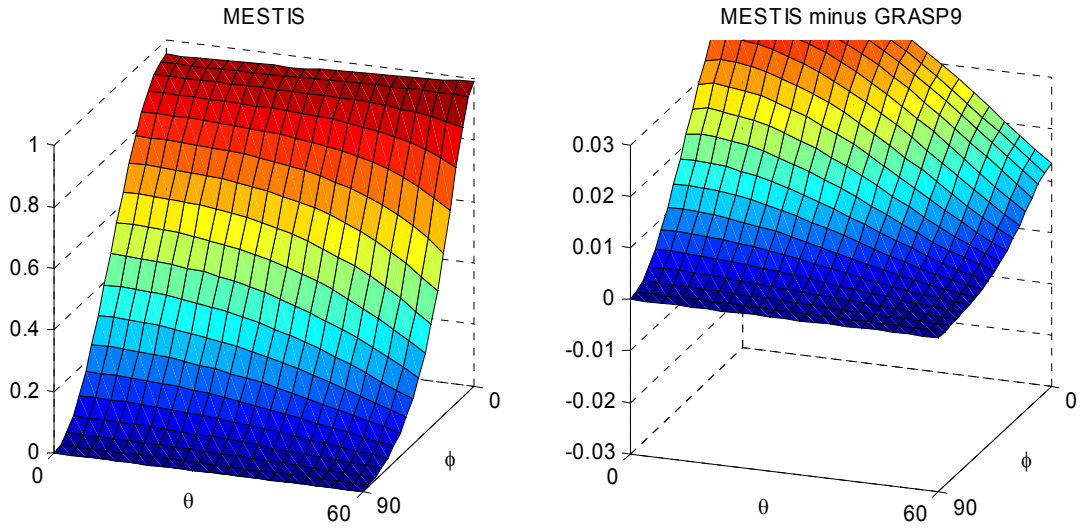

Figure 6-6 Reflection coefficient for single strip grid in free space, $s = 1.5$ mm, $w = 0.01$ mm

6.2.2 Strip grid in dielectric resin

This example uses the same strip grid as before but it is now located in the middle of a 7.5 mm thick dielectric layer with a relative dielectric constant $\varepsilon_r = 4$. This thickness was selected because it provides perfect cancellation of the reflected field for normal incidence in the absence of the strip grid.

The results for $|R_{\theta\theta}|$ are shown in Figure 6-7. This case is interesting in the sense that it illustrates the limitations of the GRASP9 approach. The reason is that in GRASP9 the result is obtained by cascading three independent layers: 1) a 3.75 mm thick dielectric, 2) the strip grid and 3) another 3.75 mm thick dielectric. In MESTIS the interaction between the strip grid and the dielectric is properly taken into account.

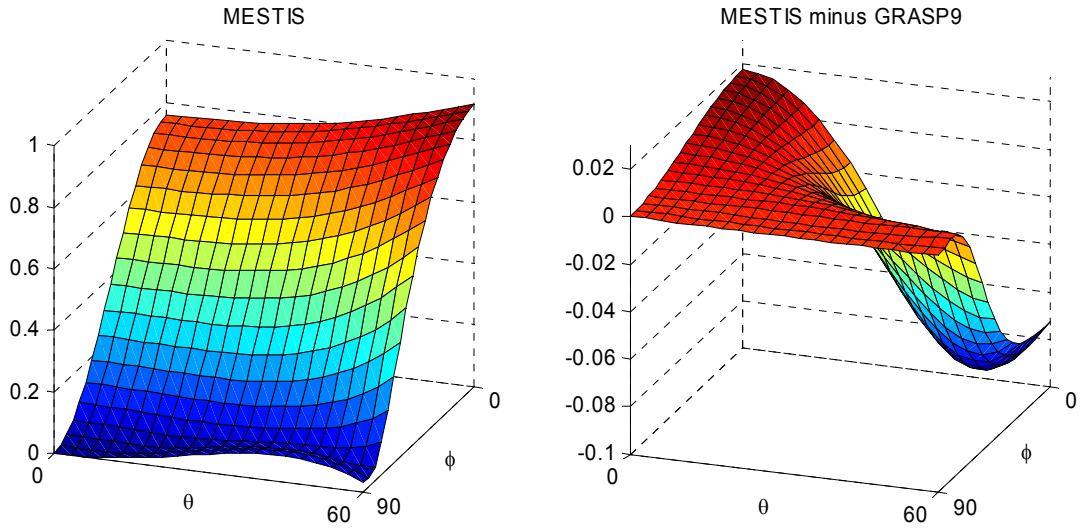

Figure 6-7 Reflection coefficient for single strip grid in the middle of a 7.5 mm thick dielectric with $\varepsilon_r = 4$, $s = 1.5$ mm, $w = 0.1$ mm

At normal incidence for $\phi = 0°$ the difference between GRASP9 and MESTIS is quite small, about 2%, but for increasing angle of incidence the difference increases rapidly. For $\phi = 90°$ the strip grid is orthogonal to the θ-direction and only the dielectric plate is playing a role and GRASP9 and MESTIS provide the same result.

6.2.3 Strip grid on a dielectric layer of varying thickness

In practice the strip grid is often laser etched into a metallic layer deposited on the one side of a dielectric supporting structure. It is therefore of interest to investigate the performance of a strip grid located directly on the one side of a dielectric sheet.

The first example is very similar to the one in the previous section but the strip grid is now moved to the top surface of the dielectric instead of being located in the middle of the sheet. The thickness of the dielectric is the same, 7.5 mm, corresponding to $\lambda/4$ (λ is the free space wavelength). The calculated results are shown in Figure 6-8.

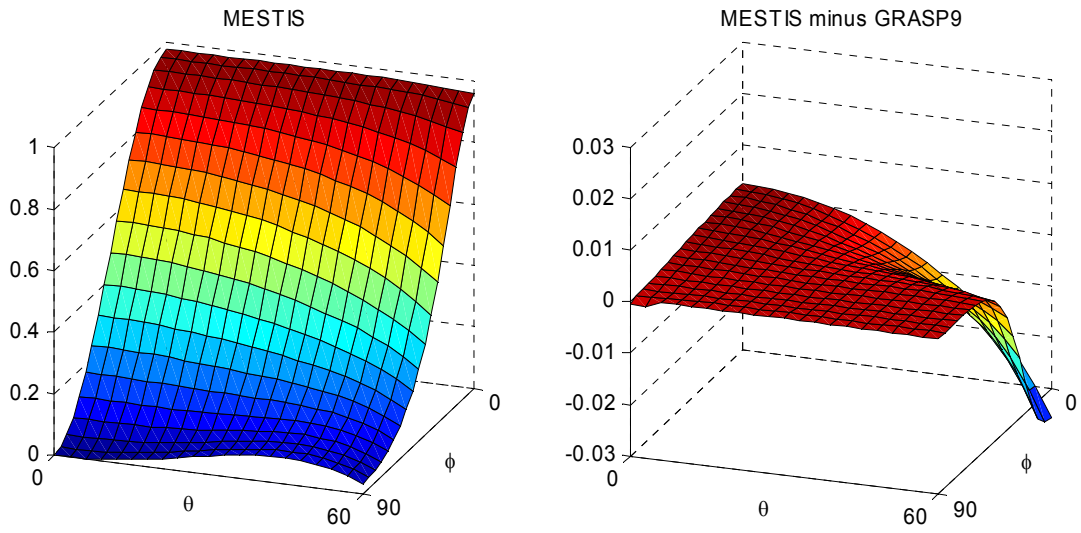

Figure 6-8 Reflection coefficient for single strip grid located on the top side of a 7.5 mm thick dielectric with $\varepsilon_r = 4$, $s = 1.5$ mm, $w = 0.1$ mm

At normal incidence the agreement between GRASP9 and MESTIS is very good, but for increasing angle of incidence and $\phi = 0°$ the difference increases rapidly. For $\phi = 90°$ the strip grid is orthogonal to the θ-direction and GRASP9 and MESTIS provide the same result.

Realistic dielectric supporting structures are much thinner than the plate in Figure 6-8. We will therefore gradually reduce the thickness of the dielectric until we get the same good agreement as for the strip grid in free space in Figure 6-4.

Figure 6-9 shows the result for a dielectric plate 3.75 mm thick. The agreement between MESTIS and GRASP9 is virtually unaffected compared to Figure 6-8.

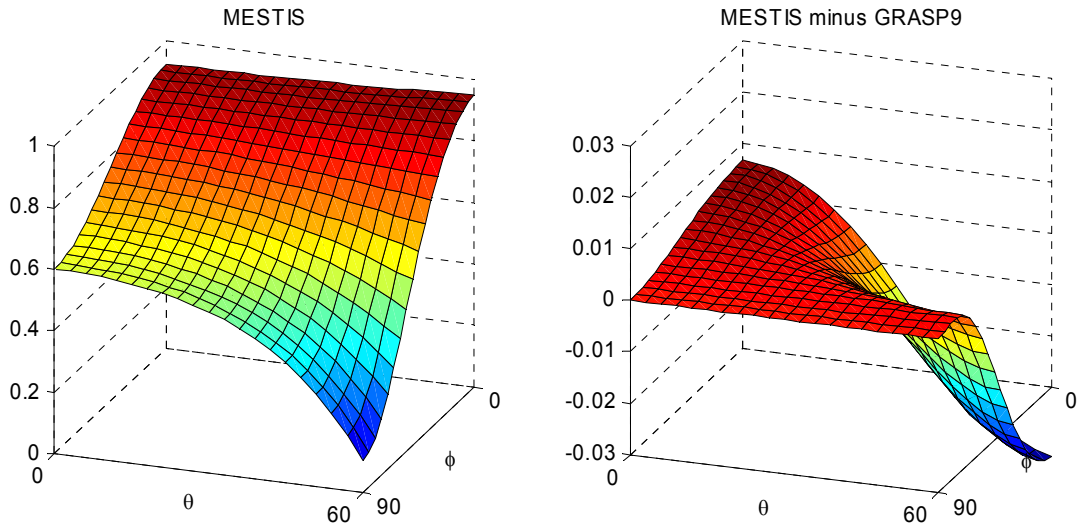

Figure 6-9 Reflection coefficient for single strip grid located on the top side of a 3.75 mm thick dielectric with $\varepsilon_r = 4$, $s = 1.5$ mm, $w = 0.1$ mm

The difference between MESTIS and GRASP9 continues to exist when reducing the dielectric thickness. Even for a thickness as small as 0.1 mm, corresponding to $\lambda/300$, we get the result in Figure 6-10. Now the difference starts to disappear when the thickness is further reduced and Figure 6-11 shows the result when the thickness is 0.01 mm ($\lambda/3000$) and the agreement is now almost as good as for the strip grid in free space, cf. Figure 6-4.

The MESTIS results presented in this section have been verified by ASG. They show that when a strip grid is located on the surface of a dielectric the approximate method in GRASP9 is good at normal incidence but it starts to deteriorate as the incidence angle increases. This behaviour is almost independent of the thickness of the dielectric until it becomes as thin as $\lambda/300$ where it starts to disappear. This discrepancy between MESTIS and GRASP9 is apparently isolated to an extremely thin layer around the strip grid and it seems likely that the GRASP9 expressions can be improved by simple means taking into account the difference in dielectric constant on the two sides of the grid.

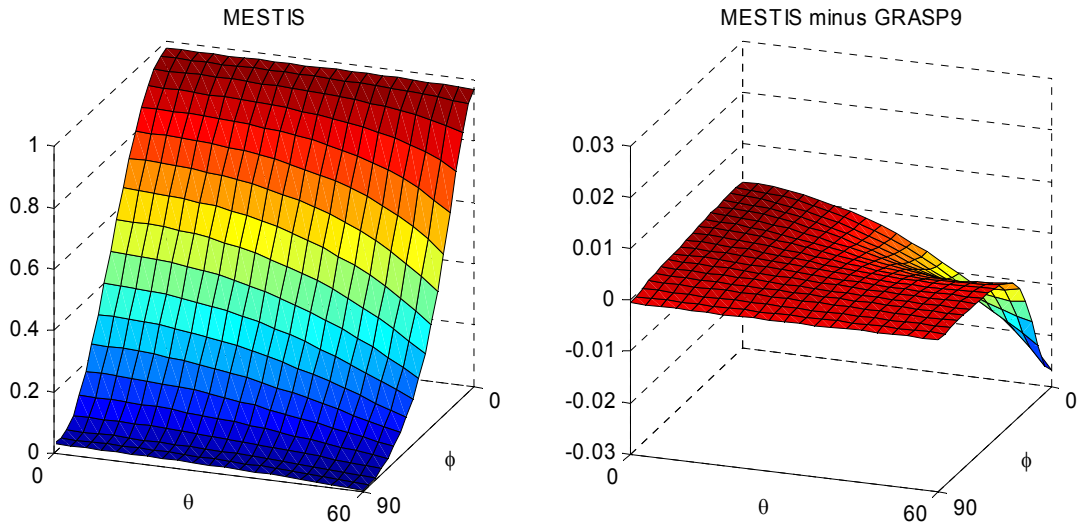

Figure 6-10 Reflection coefficient for single strip grid located on the top side of a 0.1 mm thick dielectric with $\varepsilon_r = 4$, $s = 1.5$ mm, $w = 0.1$ mm

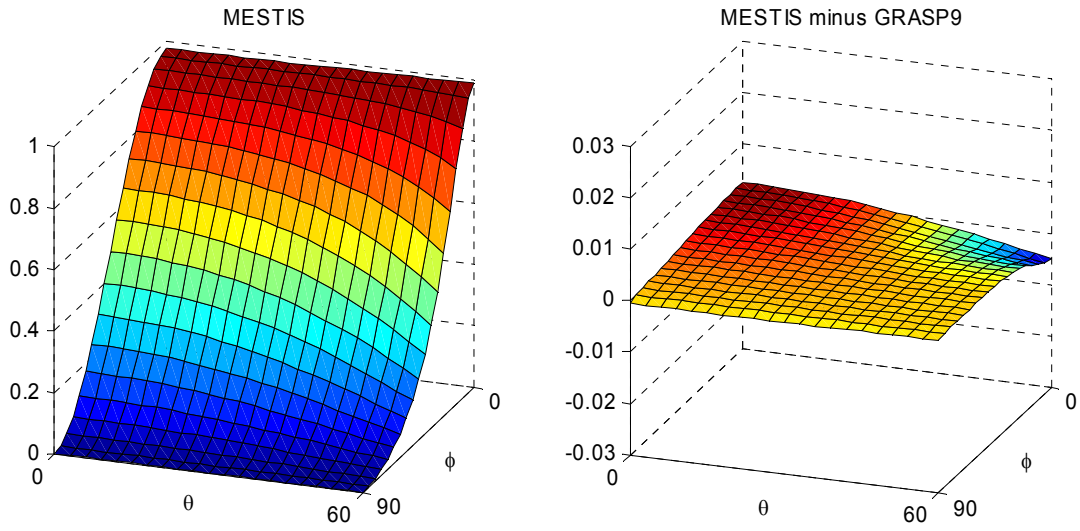

Figure 6-11 Reflection coefficient for single strip grid located on the top side of a 0.01 mm thick dielectric with $\varepsilon_r = 4$, $s = 1.5$ mm, $w = 0.1$ mm

6.2.4 Strip grid at varying heights above a dielectric layer

It was demonstrated in the previous section that the approximate formulas in GRASP9 give rise to small errors when a strip grid is located directly on the surface of a dielectric. We know from past experience that the simple formulas work well if there is a distance between the strip grid and the dielectric. It is therefore of interest to find out the lower level of this distance where we still get acceptable results.

Figure 6-12 shows the reflection coefficient for the case where the strip grid is located 4 mm above a dielectric plate, 3.75 mm thick and with a relative permittivity of 4. We see that the agreement between MESTIS and GRASP9 is very good and almost as good as for the strip grid in free space, cf. Figure 6-4.

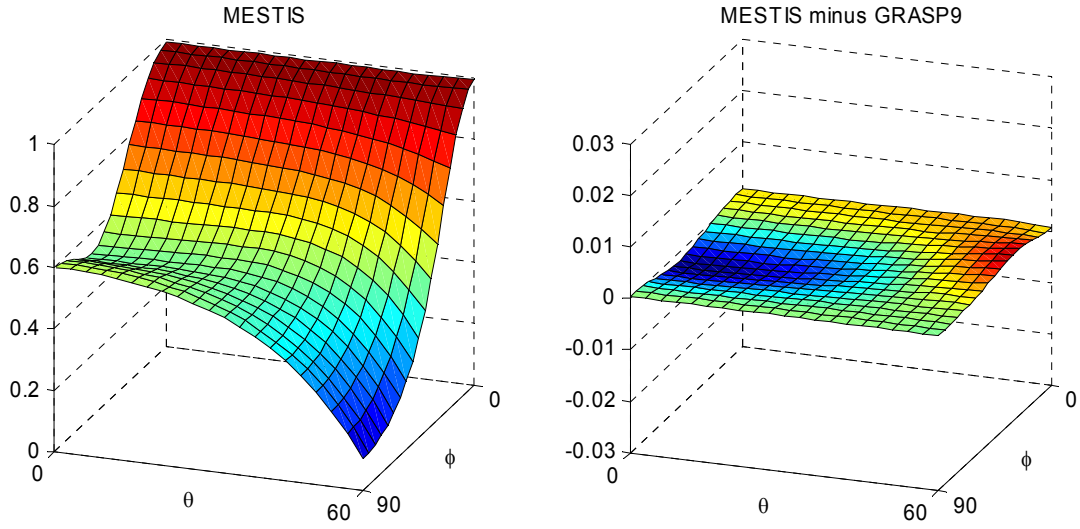

Figure 6-12 Reflection coefficient for single strip grid with $s = 1.5$ mm, $w = 0.1$ mm, located 4 mm above a 3.75 mm thick dielectric with $\varepsilon_r = 4$.

Reducing the height of the strip grid above the dielectric gradually to zero must necessarily end with the result shown in Figure 6-9. Figure 6-13 and Figure 6-14 show the results for a height of 0.3 mm ($\lambda/100$) and 0.06 mm ($\lambda/500$), respectively. It is surprising to notice, that the spacing of the strips is five times larger than the distance to the dielectric plate in Figure 6-13, but still the free space cascading used in GRASP9 works very well. In Figure 6-14 the result starts to approach the zero height result in Figure 6-9.

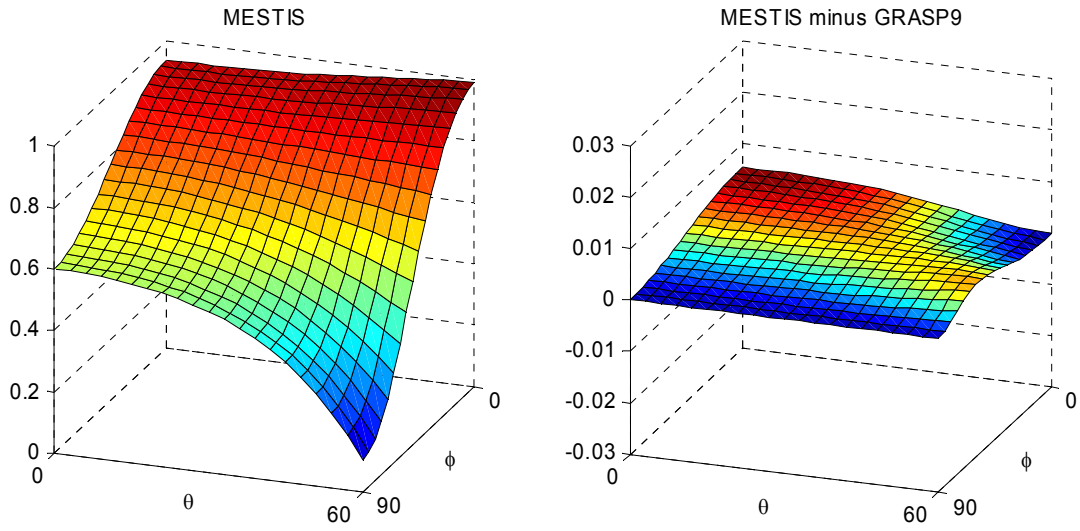

Figure 6-13 Reflection coefficient for single strip grid with $s = 1.5$ mm, $w = 0.1$ mm, located 0.3 mm $(\lambda/100)$ above a 3.75 mm thick dielectric with $\varepsilon_r = 4$.

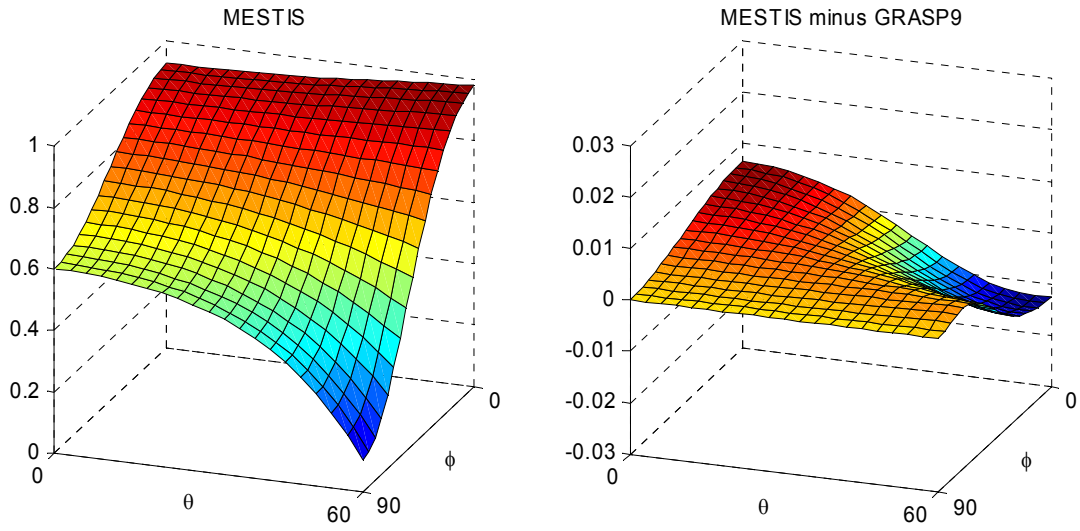

Figure 6-14 Reflection coefficient for single strip grid with $s = 1.5$ mm, $w = 0.1$ mm, located 0.06 mm $(\lambda/500)$ above a 3.75 mm thick dielectric with $\varepsilon_r = 4$.

6.3 Rectangular meshes

In this section we investigate two orthogonal strip grids in the same plane and in electrical contact at all intersection points. The parameters selected for the test case are

frequency = 10 GHz ($\lambda = 30$ mm)
spacing of x-directed strips, s_x = 1.5 mm
spacing of y-directed strips, s_y = 3.0 mm
strip width, w = 0.2 mm

and the calculated results are shown in Figure 6-15.

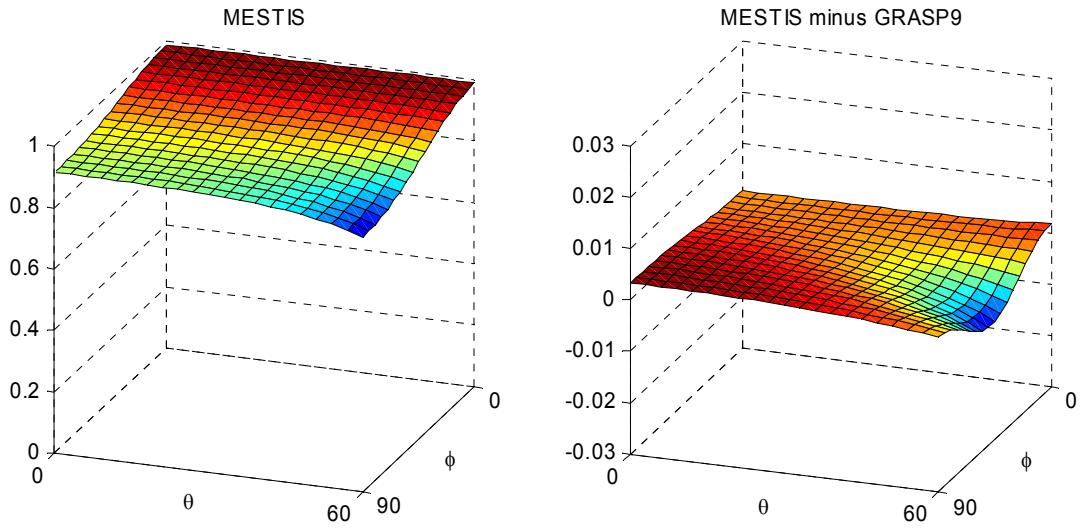

Figure 6-15 Reflection coefficient for rectangular mesh,
spacing of x-directed strips, 1.5 mm
spacing of y-directed strips, 3.0 mm
strip width, 0.2 mm

The agreement between MESTIS and the simple formulas by Astrakhan used in GRASP9 is very good. It is particularly interesting to notice that for incidence in the yz-plane, $\phi = 90°$, the reflection coefficient decreases rapidly with the angle of incidence and this is in contrast to what we have seen for single strip grids. We have therefore repeated the calculation for a single strip grid with the same parameters as for the y-directed strips of the rectangular mesh and the result can be seen in Figure 6-16. For normal incidence, $\theta = \phi = 0°$, we get the same result as for the rectangular mesh for $\theta = 0°, \phi = 90°$, but away from the normal the reflection increases. The existence of the x-directed strips of

the rectangular mesh therefore reduces the reflection rather increasing it. This property is in fact already pointed out by Astrakhan by saying that the screening properties of a rectangular mesh are best if the wires forming the mesh are insulated.

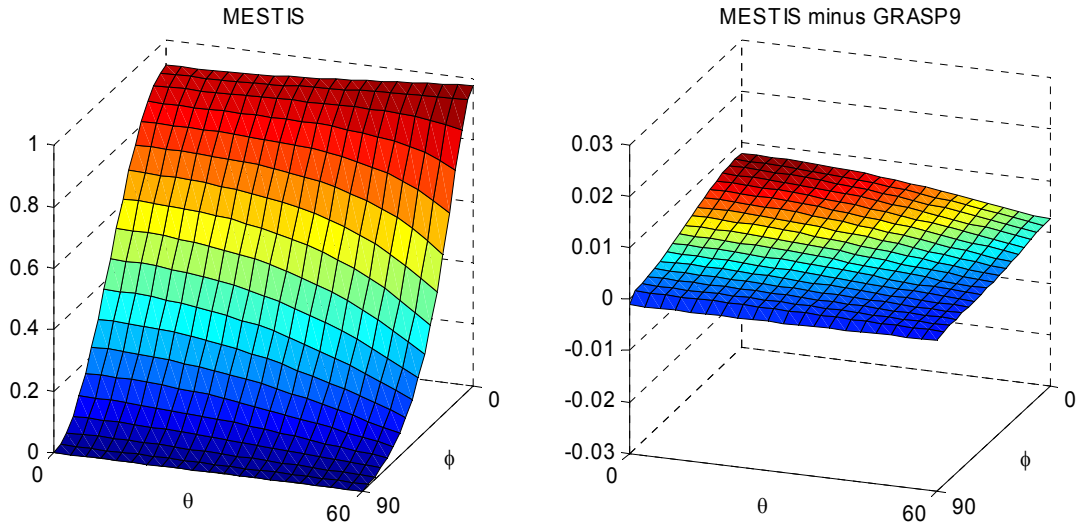

Figure 6-16 Reflection coefficient for single strip grid in free space, $s = 3.0$ mm, $w = 0.2$ mm
The $\phi = 0°$ response of this figure should be compared to the $\phi = 90°$ response of Figure 6-15.

6.4 Conclusions from Chapter 6

The results presented in this chapter have demonstrated that when a strip grid is located in free space there is a very good agreement between the simple formulas used in GRASP9 and the rigorous solution obtained by MESTIS or ASG. It has also been shown that when a strip grid is located directly on the surface of a dielectric some discrepancies occur, but when the strip grid is lifted even a very small distance above the dielectric these problems disappear again.

When a strip grid is located inside a dielectric the simple formulas break down for incidence angles other than normal incidence. However, since the simple method works well in free space it must be possible to modify it to the actual wavelength and direction of incidence inside the dielectric. This approach will work as

long as the strip grid is not too close to the front or rear surface of the dielectric.

The results presented in Section 6.2.3 showed that when a strip grid is located directly on the surface of a dielectric the approximate method in GRASP9 is good at normal incidence but it starts to deteriorate as the incidence angle increases. This discrepancy was found to be isolated to an extremely thin layer around the strip grid and it was concluded that the GRASP9 expressions can possibly be improved by simple means taking into account the difference in dielectric constant on the two sides of the grid.

6.5 References to Chapter 6

Astrakhan, 1968

H.I.Astrakhan, "Reflecting and screening properties of plane wire grids", Radio Engineering, Vol. 23, No. 1, pp. 76-83´, 1968.

ASG, 1997

"Analysis of strip gratings (ASG): User guide", CESPA-CNR, Politecnico di Torino, Torino, Italia, 1997.

Butler, 1982

Butler, "The equivalent radius of a narrow conducting strip", IEEE Trans. Antennas Propagat., Vol. AP-30, No. 4, pp. 755-758, 1982.

Nakamura and Ando, 1988

K.Nakamura and M.Ando, "A full-wave analysis of offset reflector antennas with polarization grids", IEEE Trans. Antennas Propagat., Vol. 36, No. 2, pp. 164-170, 1988.

Orta et al., 2001

R.Orta, R.Tascone and D.Trinchero, “User Manual, Metallic Strips Simulator”, Politecnico di Torino, Ref.: 012007/EM/RT, July 2001.

Pontoppidan, 2005

K.Pontoppidan, ”GRASP9 Technical Description”, TICRA Engineering Consultants, February 2005.

7 The PZM Method applied to the frequency selective radome

7.1 Introduction

Frequency selective surfaces (FSS) [1][2] are widely used for the realization of polarizers and dichroic reflectors. Due to the large dimensions of these structures, the analysis is usually performed by resorting to high-frequency techniques, such as Physical Optics (PO) or Geometrical Optics (GO), sometimes augmented by diffraction theories (PTD, UTD, ITD). In these framework, it would be desirable to have a simple and accurate surface impedance model of periodic surfaces, to be interfaced with existing high-frequency electromagnetic simulation tools.

Recently, a method has been introduced for the efficient synthesis of the FSS admittance (patch-type FSS) or impedance (aperture-type FSS) matrix, focused on the study of dispersion properties of FSS-based artificial surfaces [3][4][5]. This method is based on the application of the Foster's reactance theorem [6], which implies that FSS admittance functions of frequency satisfy the pole-zero analytical properties of the driving point LC admittance functions [7]. The identification of the poles and zeros of the FSS equivalent admittance allows a reconstruction of the surface response over a large frequency band. The FSS equivalent admittance/impedance is derived directly from the method of moment (MoM) matrix, by a proper projection onto the Floquet modes.

In this work, the method is extended to the analysis and synthesis of FSS with losses. The method allows to synthesize the scattering response of a FSS, from the identification of a few parameters (poles and residues of the equivalent FSS admittance/impedance matrix) which exhibit a weak dependence on the angle of incidence. This property implies a MoM analysis of the FSS for a limited set of incidence angles. The overall response is then interpolated with a numerically efficient algorithm. Unlike the technique described in [7], here the analytical matching of pole and zeros is substituted with an analytical matching of poles and residues; this allows the generalization of the generalized Foster's properties to all the terms of the admittance (impedance) matrix in case of losses.

This report is organized as follow. Sec. 1 provides a brief overview of the spectral domain Floquet waves (FW)-based Method of Moment, for both patch-type and aperture-type FSS. In Sec. 2, a FW-based network and the dominant mode two-ports admittance network are defined. Sec. 3 presents same important properties of the two-ports FSS-network matrices and it indicates how they can be used in order to obtain an analytical approximation of the FSS-network matrix entries. In Sec. 4 an application oriented algorithm is presented for the use of the method in conjunction with ray-tracing techniques. In Sec.5 the analytical form for the scattering matrix is conveniently used in ray-tracing algorithms, based on local flat-surface approximations of curved FSS, to evaluate the radiation pattern of an antenna enclosed by a FSS radome; numerical results obtained for the radiation pattern of the antenna radiating in free space, of the antenna enclosed by a dielectric and FSS radome are compared.

7.2 MoM Solution

Let us consider an infinite planar FSS consisting of patches printed on a multilayer dielectric slab. We will first describe the MoM analysis associated with patch-type FSS and next we will briefly present the results to aperture-type FSS obtained with a similar process. A rectangular (x,y,z) reference system is assumed with the z axis orthogonal to the FSS and the origin at the FSS level. The periodicities of the FSS are dx and dy along x and y, respectively. An incident, either transverse electric (TE) or transverse magnetic (TM), plane wave is assumed to illuminate the structure, with zero phase at the origin of the reference system. The incident plane wave imposes a phasing kx and ky in the principal directions, with $k_x^2 + k_y^2 < \omega^2 / c^2$.

The numerical computation of the equivalent currents at the interface of the planar periodic structure is performed via a numerical solution of the electric field integral equation (EFIE) by using a spectral periodic MoM approach. More than discussing the numerical implication of the MoM scheme, our objective here is to construct an appropriate form of the admittance matrix to characterize the FSS surface.

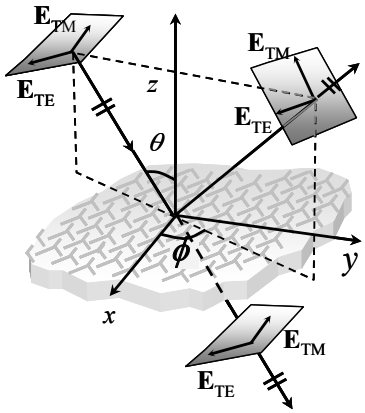

Fig. 1 A planar patch-type FSS and relevant plane wave excitation for TE and TM polarization.

Due to the periodicity of the problem, the analysis can be reduced to that of a single periodic cell, with phase-shift boundary conditions applied to the ideal vertical walls. By applying the equivalence theorem (Fig. 2), an electric current distribution is assumed on the region of the metallic patches, radiating with the Green's function (GF) of the grounded slab. By imposing the boundary conditions on the surface of the metallic patches, the EFIE is derived, as follows:

$$\mathbf{E}_s\left(\mathbf{J}\right)+\mathbf{E}_{imp}=0 \tag{1}$$

where Es is the field radiated by the currents J induced on the dipoles, and Eimp = Einc+Eref is the impressed field at the interface (in the absence of printed dipoles), which is given by the sum of the incident (Einc) and reflected (Eref) fields. From here on, the bold characters indicate vectors and the carets indicate unit vectors. As suggested by Tascone and Orta in [2], the equivalent currents J are expressed in terms of basis functions,

$$\mathbf{J}(\mathbf{r_t})=\sum_{n=1}^{N} I_n\ \mathbf{f}_n(\mathbf{r_t}) \tag{2}$$

where $\mathbf{r}_t = x\hat{x}+y\hat{y}$ denotes the two-dimensional space vector. Fig. 2 shows sub-domain triangular basis functions, but entire domain basis functions can be used as well.

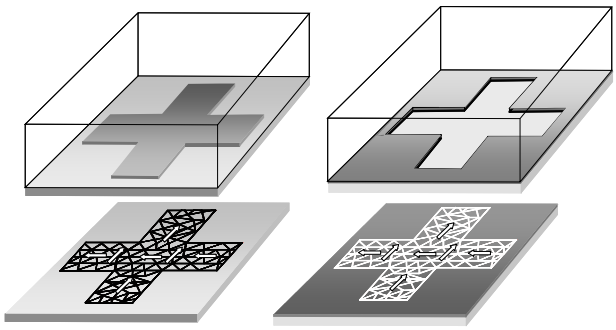

Fig. 2 Application of the equivalence principle to the basic cell of (a) patch-type FSS and (b) aperture-type FSS. Phase shift conditions are imposed on the vertical walls. A triangular mesh is shown, with sub-domain basis functions used for the expansion of the electric.

Let us denote by $k_{xp'}=k_x+2\pi p'/d_x$, $k_{yq'}=k_y+2\pi q'/d_y$ the FW wavenumbers in the x and y direction, respectively, and by $\mathbf{k}_q=k_{xp'}\hat{x}+k_{yq'}\hat{y}$ the relevant vector form, where q denotes the two FW indices (p',q').

By denoting with $\boldsymbol{\beta}_q$ the nodes of the reciprocal lattice, $\boldsymbol{\beta}_q = \frac{2\pi p'}{d_x}\hat{x} + \frac{2\pi q'}{d_y}\hat{y}$, and with k the impressed vector wavenumber, $\mathbf{k} = k_x\hat{x} + k_y\hat{y}$, we obtain $\mathbf{k}_q = \mathbf{k} + \boldsymbol{\beta}_q$, with q=0, 1, 2… and $\mathbf{k}_0 = \mathbf{k}$ by definition. It is also useful to introduce the normalized spectral vectors

$$\hat{\sigma}_q = \frac{\mathbf{k}_q}{\sqrt{\mathbf{k}_q \cdot \mathbf{k}_q}} \quad ; \qquad \hat{\alpha}_q = \hat{z} \times \hat{\sigma}_q \tag{3}$$

as a spectral basis to describe TM and TE field components, respectively. By using a Galerkin spectral MoM approach, Eq. (1) is reduced to the matrix equation

$$\overline{\overline{Z}}_{MOM}\, \overline{I} = \overline{V} \tag{4}$$

where $\overline{V} = \{V_m\}^T_{m=1,N}$ is the known column vector of the complex amplitude of the impressed field on the $\mathbf{f}_n$ basis, $\overline{I} = \{I_n\}^T_{n=1,N}$ is the column vector of the current expansion, and $\overline{\overline{Z}}_{MoM} = \left\{Z^{MoM}_{nm}\right\}_{n,m=1,N}$ is the MoM impedance matrix, with entries given in an appropriate TE/TM form via

$$Z^{MoM}_{mn} = \sum_{q=0}^{M-1} \tilde{\mathbf{F}}^*_m(\mathbf{k}_q) \cdot [Z^{TM}_{GF}(\mathbf{k}_q)\hat{\sigma}_q\hat{\sigma}_q + Z^{TE}_{GF}(\mathbf{k}_q)\hat{\alpha}_q\hat{\alpha}_q] \cdot \tilde{\mathbf{F}}_n(\mathbf{k}_q) \tag{5}$$

In (5), $\tilde{\mathbf{F}}_n(\mathbf{k})$ $[\tilde{\mathbf{F}}_m(\mathbf{k})]$ is the Fourier transform of the basis [test] function $\mathbf{f}_n(\mathbf{r_t})$ $[\mathbf{f}_m(\mathbf{r_t})]$, sampled at the FW wavenumbers $\mathbf{k}_q$, and $Z^{TM/E}_{GF}(\mathbf{k})$ are the TM/TE components of the individual element spectral electric field GF, sampled at the vector FW wavenumber $\mathbf{k}_q$. In (5), the modal FW expansion is truncated at the integer M-1 with M larger than N; this is an obvious consequence of the continuity of the FW on the entire periodicity cell, which implies the use of more FW modes than basis functions to describe the patch current. The GF impedances can be found by solving the pertinent transmission line problem representing the stratification for the TE and TM case. The MoM matrix can be expressed in the compact form as

$$\overline{\overline{Z}}_{MoM} = \overline{\overline{Q}}^{H}\, \overline{\overline{Z}}_{GF}\, \overline{\overline{Q}} \tag{6}$$

where $\overline{\overline{Z}}_{GF} = diag\left\{Z^{TM}_{GF}(\mathbf{k}_q), Z^{TE}_{GF}(\mathbf{k}_q)\right\}_{q=0,M-1}$ is a diagonal $2M \times 2M$ matrix, $\overline{\overline{Q}} = \left\{Q^{TM}_{q,n},\ Q^{TE}_{q,n}\right\}_{\substack{q=0,M-1\\ n=1,N}}$ is a $2M \times N$ matrix and $\overline{\overline{Q}}^{H} = \left\{Q^{TM*}_{m,q},\ Q^{TE*}_{m,q}\right\}^T_{\substack{m=1,N\\ q=0,M-1}}$ is an $N \times 2M$ matrix, the superscript H denoting transpose conjugate. The entries of the Q matrices are given by $Q^{TM}_{i,q} = \tilde{\mathbf{F}}_i(\mathbf{k}_q) \cdot \hat{\sigma}_q$, $Q^{TE}_{i,q} = \tilde{\mathbf{F}}_i(\mathbf{k}_q) \cdot \hat{\alpha}_q$ (i=n,m).

For an aperture-type FSS, the FSS is substituted by a continuous, infinitely thin PEC screen with magnetic current distribution on both sides; these currents have equal amplitude and opposite signs on the two different sides to ensure the continuity of the electric field through the aperture. The integral equation which imposes the continuity of the magnetic field is $\mathbf{H}^+_s(\mathbf{M}) + \mathbf{H}_{imp} = \mathbf{H}^-_s(-\mathbf{M})$, where the superscript + and – refer to the Green's function of the upper and lower region, respectively. The magnetic current is expanded in terms of basis functions

$$\mathbf{M}(\mathbf{r_t}) = \sum_{n=1}^{N} V_n \mathbf{g}_n(\mathbf{r_t}) \times \hat{z} \tag{7}$$

Imposing the continuity of the magnetic field leads to the following representation

$$\overline{\overline{Y}}_{MoM}\, \overline{V} = \overline{I} \tag{8}$$

where $\overline{V} = \{V_n\}^T_{n=1,N}$ is the unknown column vector, $\overline{I} = \{I_m\}^T_{m=1,N}$, $I_m = -\tilde{\mathrm{G}}^*_m(\mathbf{k}) \cdot \mathrm{H}_{imp}(\mathbf{k})$ is the known column vector of the impressed magnetic field on the MoM basis. The MoM matrix may be expressed in the compact form

$$\overline{\overline{Y}}_{MoM} = \overline{\overline{P}}^{H}\, \overline{\overline{Y}}_{GF}\, \overline{\overline{P}} \tag{9}$$

where $\overline{\overline{Y}}_{GF} = diag\left\{Y_{GF}^{TM}(\mathbf{k}_q), Y_{GF}^{TE}(\mathbf{k}_q)\right\}_{q=1,M} = \overline{\overline{Z}}_{GF}^{-1}$ is a diagonal $2M \times 2M$ matrix, obtained by solving the GF z-transmission line for each FW wavevector, $\overline{\overline{P}}^{H} = \left\{P_{m,q}^{TM*},\ P_{m,q}^{TE*}\right\}_{\substack{m=1,N \\ q=0,M-1}}^{T}$ is an $N \times 2M$ matrix, and $\overline{\overline{P}} = \left\{P_{q,n}^{TM},\ P_{q,n}^{TE}\right\}_{\substack{q=0,M-1 \\ n=1,N}}$ is a $2M \times N$ matrix, whose components are given by $P_{i,q}^{TM} = \tilde{\mathbf{G}}_i(\mathbf{k}_q) \cdot \hat{\sigma}_q$, $Q_{i,q}^{TE} = \tilde{\mathbf{G}}_i(\mathbf{k}_q) \cdot \hat{\alpha}_q$ (i=n,m), being $\tilde{\mathbf{G}}_i(\mathbf{k})$ the Fourier transform of $\mathbf{g}_i(\mathbf{r}_t)$.

7.3 Dominant-mode two-port admittance network

Let us assume that we are observing the field at a certain distance z from the FSS. In this case, the FW modes that are completely attenuated do not contribute to the field at z. In a multimode network description, this implies that the relevant modal ports can be considered as not "accessible" to the observer, and therefore neglected. This concept was introduced by Rozzi [8] for waveguide problems and is commonly used to calculate the coupling between FSSs located at different levels [2]. When we are dealing with the scattering from an FSS, the only accessible mode is the propagating one. Consider the 2-port network in Fig. 3, where each port is associated to an FW mode of TE or TM type. This network consists of a 2-port "FSS network" loaded in parallel at each port by a modal TE or TM transmission line representing the unprinted multilayer dielectric slab. The FSS-network is conveniently characterized by 2×2 admittance (impedance) matrices

$$\overline{I}_{FW}^{FSS} = \overline{\overline{Y}}_{FSS}\,\overline{V}_{FW} \tag{10}$$

for patch-type FSS

$$\overline{V}_{FW} = \overline{\overline{Z}}_{FSS}\,\overline{I}_{FW}^{FSS} \tag{11}$$

for aperture-type FSS, where $\overline{I}_{FW}^{FSS} = [I_{FW,q}^{TM}, I_{FW,q}^{TE}]_{q=0,1}^{T}$ ($\overline{V}_{FW} = [V_{FW,q}^{TM}, V_{FW,q}^{TE}]_{q=0,1}^{T}$), is the vector of the FW amplitudes of the magnetic (electric) field expansion at the FSS level and denotes the FW electric current flowing into the FSS network (the FW voltage at the ports).

The FSS-network matrices are given as a function of $\overline{\overline{Z}}_{MoM}$ matrix as

$$\overline{\overline{Y}}_{FSS}(k_x, k_y; \omega) = \overline{\overline{q}} \left(\overline{\overline{Z}}_{MoM}\right)^{-1} \overline{\overline{q}}^{H} \left[\overline{\overline{Y}}_{GF} - \overline{\overline{q}} \left(\overline{\overline{Z}}_{MoM}\right)^{-1} \overline{\overline{q}}^{H}\right]^{-1} \overline{\overline{Y}}_{GF} \tag{12}$$

for patch-type FSS, and $Y_0^{TM}(\mathbf{k})$, $Y_0^{TE}(\mathbf{k})$; $Y_1^{TE}(\mathbf{k})$ $Y_1^{TM}(\mathbf{k})$ are the modal z-transmission line TE-TM characteristic admittances relevant to the free-space (subscript 0) and the dielectric regions (subscript 1), respectively, and $k_z = \sqrt{k^2 - k_x^2 - k_y^2}$ and $k_{z1} = \sqrt{\varepsilon_r k^2 - k_x^2 - k_y^2}$

$$\overline{\overline{Z}}_{FSS}(k_x, k_y; \omega) = \overline{\overline{p}} \left(\overline{\overline{Y}}_{MoM}\right)^{-1} \overline{\overline{p}}^{H} \left[\overline{\overline{Z}}_{GF} - \overline{\overline{p}} \left(\overline{\overline{Y}}_{MoM}\right)^{-1} \overline{\overline{p}}^{H}\right]^{-1} \overline{\overline{Z}}_{GF} \tag{13}$$

for aperture-type FSS. In (12)- (13), the dependence on the frequency and on the impressed wave vector has been emphasized, and $\overline{\overline{q}} = \left\{Q_{q,n}^{TM},\ Q_{q,n}^{TE}\right\}_{\substack{q=0,M_A-1 \\ n=1,N}}$, $\overline{\overline{p}} = \left\{P_{q,n}^{TM},\ P_{q,n}^{TE}\right\}_{\substack{q=0,M_A-1 \\ n=1,N}}$, are matrices of size $2M_A \times N$ which project the MoM basis onto the FW basis (and vice versa for their transpose conjugate $\overline{\overline{q}}^{H}$ and $\overline{\overline{p}}^{H}$.

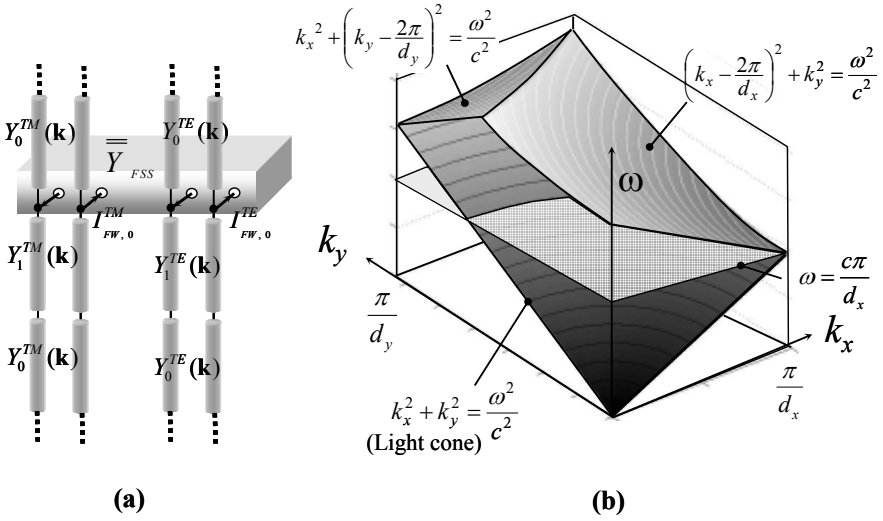

Fig. 3 (a), Two-port modal network relevant to propagating the TE and TM FW-mode. (b) Diagram $(k_x,k_y)-\omega$ (the figures refer to a case dx > dy).Below the two portions of the upper conical surfaces, the higher order FW modes are cut off. This region identifies the validity of the FSS-network in (a). The free-space speed of light is denoted by c. The "light cone" is also depicted, and its surface identifies the cut-off of the dominant propagating mode.

As previously stated, the utilization of a two-port network, implies that all the higher-order FW-modes must be cut off. The cut-off condition of the higher-order FW-modes implies a limitation to the observable dispersion diagram. Figure 4b shows a dispersion diagram with angular frequency ω on the vertical axis and the wavenumbers *kx*, and *ky* on the horizontal axes. Due to the periodicity of the FW spectrum, the observation may be restricted to the Brillouin region $(-\pi/d_x<k_x<\pi/d_x,-\pi/d_y<k_x<\pi/d_y)$, with a further (due to the symmetry of the structure) restriction to positive values of *kx* and *ky*. The cut-off region for higher-order modes is imposed by the conditions $k_{x\xi}^2+k_{y\eta}^2>\omega^2/c^2$ for $(\xi,\eta)\neq(0,0)$. As a consequence, within the observed wavenumber plane, the cut-off region is delimited by portions of two cones whose vertices are at the FW wavenumbers closest to the origin (details are shown in Fig. 4b). A third cone is depicted in the same figure; its surface $k_x^2+k_y^2=\omega^2/c^2$ defines the cut-off of the dominant mode. Although this cone is not essential for the validity of the two-port model, it bounds the slow-wave region and is important for the study of the dispersion properties. Intersections of this cone with the vertical planes ω-kx and ω-ky identify the well-known "light lines" in these two planes. Figure 4b also shows the horizontal plane $\omega=\omega_M=c\pi/\max(d_x,d_y)$, which is the minimum frequency at which the higher-order FW modes are attenuated for any wavenumber.

7.4 Properties of FSS-network matrix entries

Here we describe the properties of the two-port FSS matrix entries in order to establish a convenient analytical form. For the sake of convenience, let as consider each element of the matrix as a function dependent on θ and ϕ, where $k_x=k_0\sin\theta\cos\phi$ and $k_y=k_0\sin\theta\sin\phi$. In this case, the cut-off region shown i3.4.3. n Fig. 3b can be expressed as a function of θ and ϕ, obtaining the surfaces presented in Fig. 4.

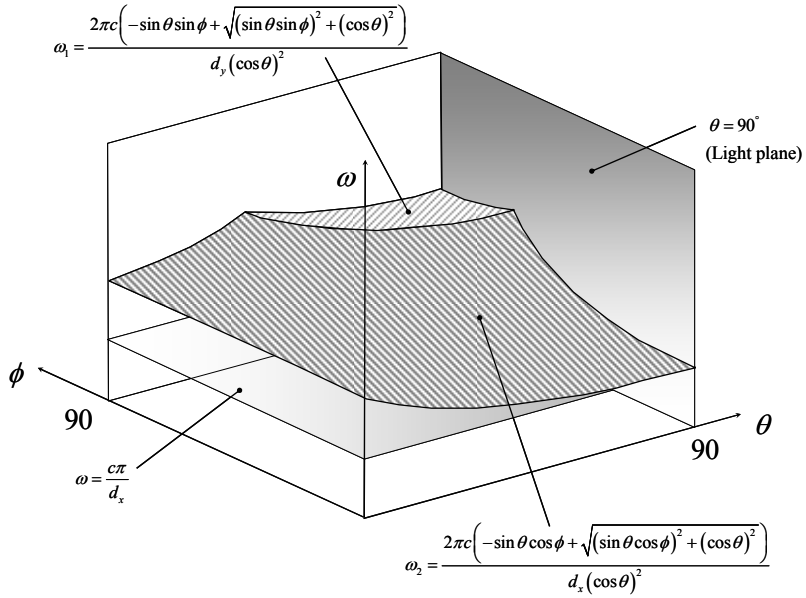

Fig. 4 Mono-modal propagation region for the fundamental FW $(\theta,\phi)-\omega$ (the figures refer to a case dx > dy).Below the two portions of the upper surfaces $\omega_1(\theta,\phi)$ and $\omega_2(\theta,\phi)$, the higher order FW modes are cut off. This region identifies the validity of the FSS-network in Fig.4(a). The free-space speed of light is denoted by c. The "light plane" is also depicted, and its surface identifies the cut-off of the dominant propagating mode.

7.4.1 Absence of losses

Consider for simplicity the patch-type FSS and denote by $Y_{FSS}^{ij}(\theta,\phi,\omega)$ the entries of the two-port dominant mode admittance matrix. In the absence of losses, the equivalent FSS admittance is purely reactive for every ω. Note that this is valid within the cut-off region of the higher-order FW-modes described in Fig. 4; indeed, for frequency where another pair of TE-TM modes is propagating, the two-port FSS matrix loses its properties to be purely reactive. The imaginary part of the (purely imaginary) entries, seen as a function of frequency, possesses the same pole structure of a passive LC admittance matrix, with capacitive behavior at low frequency. Moreover, from network theory, it can be demonstrated that all the entries of the FSS-network matrix have the same poles [9]. Thus, the properties of the FSS matrix entries are

- All the entries $Y_{FSS}^{ij}(\theta,\phi,\omega)$ possess the same poles;
- The poles lie on the real ω-axis and are simple;
- A zero must be in $\omega = 0$;
- The poles are symmetrically displaced with respect to the origin;

An important consequence of these properties is that the admittance frequency function can be approximated by the following limited-bandwidth expression

$$Y_{FSS}^{ij}(\theta,\phi,\omega) = \sum_{n=1}^{N} \frac{-2ja_n^{ij}(\theta,\phi)\omega}{\omega^2-\beta_n^2(\theta,\phi)} + ja_0^{ij}(\theta,\phi)\omega \tag{14}$$

In (14) the following properties hold

$a_n^{ij}(\theta,\phi)$ represents the (ω-independent) residue associated to the n-th pole in the ω-plane and it is a real function of the incident angle. For the diagonal entries $a_n^{ii}(\theta,\phi)$ is real and positive;

7.4.2 Small losses

In the case of small losses, each FSS network matrix entry can be approximated as

$$Y_{FSS}^{ij}\left(\theta,\phi,\omega\right)=\sum_{n=1}^{N}\frac{-2ja_n^{ij}\left(\theta,\phi\right)\omega}{\omega^2-\beta_n^2\left(\theta,\phi\right)-j\omega\gamma_n\left(\theta,\phi\right)}+ja_0^{ij}\left(\theta,\phi\right)\omega \tag{15}$$

Same expression can be written for $Z_{FSS}^{ij}\left(\theta,\phi,\omega\right)$ entries for aperture-type FSS.

In (15) small losses have been assumed, i.e. $\beta_n\left(\theta,\phi\right)>>\gamma_n\left(\theta,\phi\right)$, so that $-\gamma_n\left(\theta,\phi\right)/2$ and $\beta_n\left(\theta,\phi\right)$ are the real and imaginary part of the pole respectively. Under the small losses assumption the poles are very close to the real ω-axis and their position in the complex ω-plane can be evaluated from the real axis frequency variation of the imaginary part of the matrix entries. The following properties are verified:

$a_n^{ij}\left(\theta,\phi\right)$ represents the ω-independent residue associated to the n-th pole and in the ω-plane it is a real function of the incidence angle. For diagonal entries $a_n^{ii}\left(\theta,\phi\right)$ real and positive;

The quantities $a_0^{ii}\left(\theta,\phi\right),a_\infty^{ii}\left(\theta,\phi\right)$ are independent on ω and represent the quasi-static capacitance (inductance) of the patch-type (aperture type) FSS. Their dependence on $\left(\theta,\phi\right)$ is found to be very weak and thus very easy to approximate;

Equation (1.15) allows an analytical definition of the admittance (impedance), over a broad frequency range, on the basis of the determination of the aspect-dependent poles and residues. As will be discussed later on, they can be calculated for a few values of the incidence angles , and can then be approximated.

We note that the numerical calculation of $\overline{\overline{Y}}_{FSS}$ in (15) is accurate at those angles where $\overline{\overline{Y}}_{FSS}$ exhibits poles or zeros, because the MoM matrix is there well-conditioned.

7.5 Approximation of poles and residue

From the approximation (15), the analytical representation of the FSS in a broad frequency range can be derived from the following functions

$$a_n^{ij}\left(\theta,\phi\right),\beta_n\left(\theta,\phi\right),\gamma_n\left(\theta,\phi\right),a_0^{ij}\left(\theta,\phi\right) \tag{16}$$

In many practical cases, the poles that should be considered are very few. As a practical rule the approximation is very good if one includes the poles within the frequency range of interest plus the closer one outside the same range. Since in many cases the properties of the FSS are used at low frequency regime or close to the first resonance, the inclusion of one or two poles is satisfactory in most of the cases.

All the functions in (16) show a very weak variation against the incidence angles and are easy to approximate from the data related to a few angular samples by a simple trigonometric polynomial form

$$\Psi_n^{ij}(\theta,\phi)=\sum_{n_1=0}^{N_1}\sum_{n_2=0}^{N_2}\left[\delta_{n_1n_2}\cos(n_2\phi)\cos(2n_1\theta)+\eta_{n_1n_2}\sin(n_2\phi)\sin(2n_1\theta)\right] \tag{17}$$

where $\delta_{n_1n_2}$ and $\eta_{n_1n_2}$ are coefficients calculated on the basis of a least mean square approximation. In many practical cases, N_1 and N_2 are very small integer numbers.

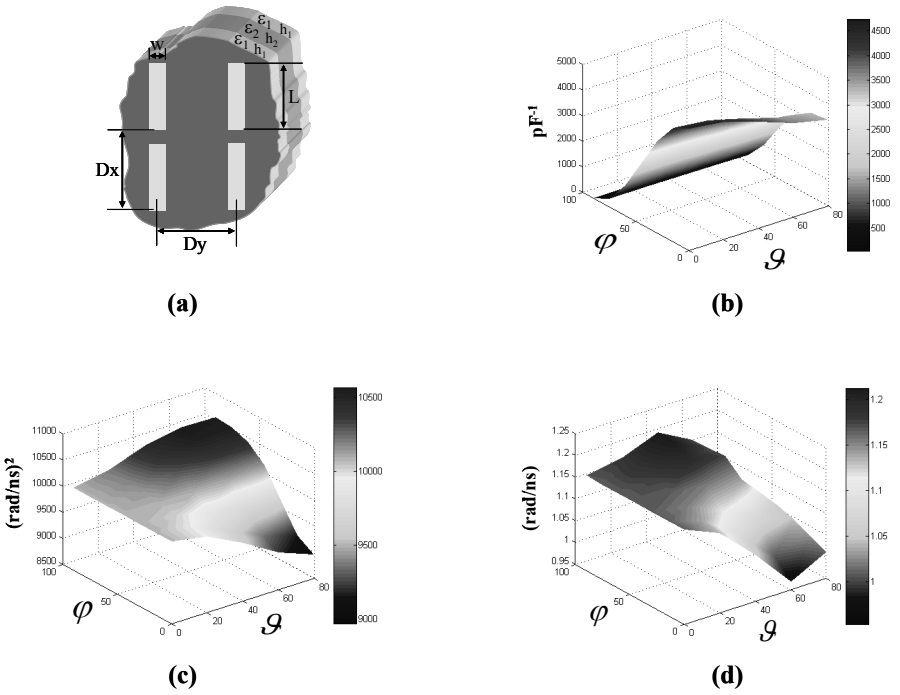

Fig. 5 Approximated poles and residue surfaces for a ring-dipole FSS. (a) Structure layout; Dx= 0.38λ_0, Dy= 0.4λ_0, L= 0.3λ_0, w= 0.06λ_0 (b) Approximated surfaces for a residue $a_2^{11}(\theta,\phi)$. (c) An example of an approximated surfaces for the real part of one pole $\beta_2^{11}(\theta,\phi)$ and (d) for the imaginary part of one pole $\gamma_2^{11}(\theta,\phi)$. For all this function the approximated surfaces have been evaluated with N_1=2 and N_2=1.

7.6 Application-oriented algorithm

The analysis of curved FSS reflectors or frequency selective radomes, which are large in terms of a wavelength, are often based on the flat surface approximation of the local curved structure and on the decomposition of the illuminating wave in terms of local rays or beams. This schemes use local reflection and transmission coefficients to calculate local currents or scattered fields, thus requiring the calculation of the scattering matrix for a large number of incident aspects and frequencies. The pole-residue method described here allows an agile transmission of data from a EM solver for the analysis of FSS and a EM solver based on high-frequency (HF) method (e.g. Physical Optics, Geometric Optics, etc..). The present polo-residue matching scheme, thanks to the capability to reconstruct an analytical form of the admittance matrix, with the use of few parameters, establishes a link from the FSS solver and the HF solver by exchanging data relevant to the few interpolation coefficients. The logical scheme of this data exchange is shown in Fig.6. Data, relevant to an angular under sampling of the FSS matrix entries, feed a "Data Compressor" which calculates the coefficients of the least mean square approximation of poles and residues. The coefficients $\delta_{n_1 n_2}$ and $\eta_{n_1 n_2}$ are thus transmitted to the HF solver which is provided by a "Decoder Module". This module constructs the analytical form of $\overline{\overline{Y}}_{FSS}(\theta,\phi,\omega)$ over continuous angles and frequencies. From this latter matrix, the scattering matrix is obtained from simple algebraic manipulations. This scheme does not alter the internal architecture of the solvers and implies a pre-processing time which is negligible with respect to the overall calculation time.

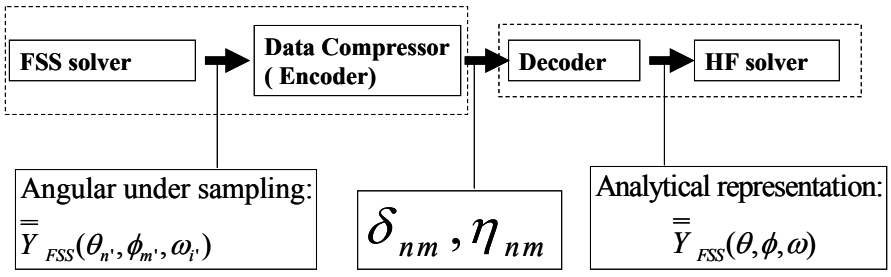

Fig. 6 Logical structure of the data compression algorithm.

7.7 Numerical results for a FSS radome

In order to analyze the impact of the FSS radome on the antenna performance, curvature effects must be included in the analysis. However, a rigorous study poses serious mathematical problems, forcing the use of approximate techniques. The reciprocity theorem is applied to estimate the pattern of the antenna enclosed by the FSS radome as the reaction between the current distribution on the antenna surface and the field transmitted through the radome when illuminated by an incident plane wave. Under the hypothesis of electrically large radome, the transmitted field is computed by ray techniques, taking into account the presence of the radome through a dyadic transmission matrix. An analytical expression of this latter, describing its dependence on the incidence angle and frequency, is obtained through a generalization of the Pole-Residue Matching method as described above.

The FSS geometry consists on a rectangular lattice with Dx= $0.38\lambda_0$ and Dy= $0.4\lambda_0$. The basic element of the FSS is a rectangular slot with a length L= $0.3\lambda_0$ and a width w= $0.06\lambda_0$, where λ_0 is the wavelength of the free space at the frequency f_0. FSS layout is shown in Fig. 7. The FSS has been designed in order to be transparent at the operating frequency f_0 of the antenna; in this way the slot FSS operates has a pass-band filter around frequency f_0.

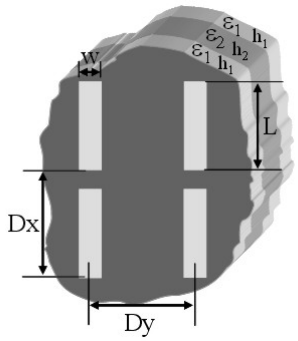

Fig. 7 FSS layout.

When a plane wave, at frequency f_0, impinges on the structure (antennas covered by a radome), with an electric field polarization orthogonal to the slot orientation, the module and the phase of the electric field transmitted on the antenna's plane are like that shown in Fig.8 and Fig.9. In particular Fig.8 shows the results for a dielectric radome, while Fig.9 those for a FSS radome.

As we can see, at the operating frequency f_0, the copolar componens of the transmitted field are approximately the same either for the module or for the phase in both cases; concerning the cross-polar component they are more than 15dB down the copolar one.

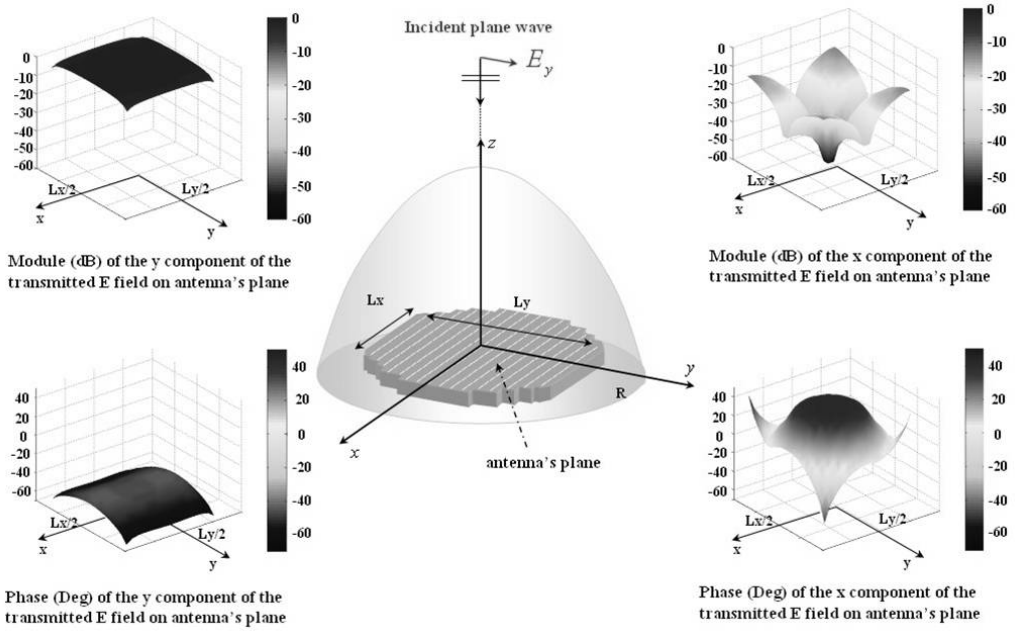

Fig. 8 Module and phase of the electric field components transmitted on the antenna's plane by a dielectric radome for an impinging plane wave with electric field polarized along y direction (orthogonal to slot direction) at the frequency f_0.

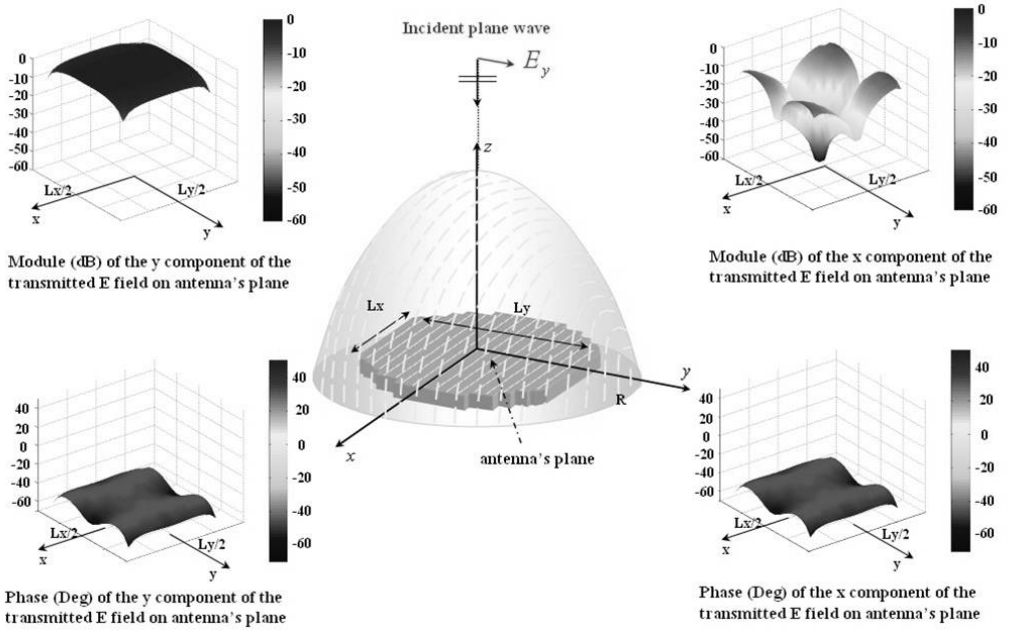

Fig. 9 Module and phase of the electric field components transmitted on the antenna's plane by a FSS radome for an impinging plane wave with electric field polarized along y direction (orthogonal to slot direction) at the frequency f_0.

In Fig.9 it is possible to see the polarization selectivity of the FSS radome for an impinging plane wave with electric field polarization parallel to the slot direction, at the frequency f_0. Outside the pass-band of the FSS, the frequency selective behaviour of the FSS radome is shown in Fig.

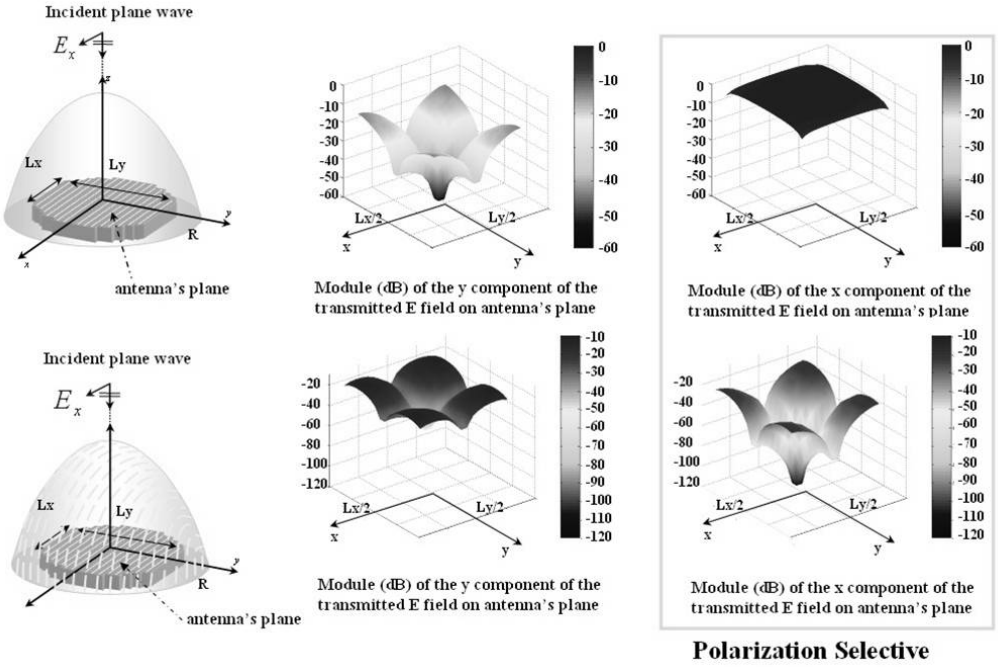

Fig. 10 Comparison between the module the electric field components transmitted on the antenna's plane by dielectric radome (upper part of the figure) and a FSS radome (lower part of the figure) for an impinging plane wave with electric field polarized along x direction (parallel to slot direction) at the frequency f_0.

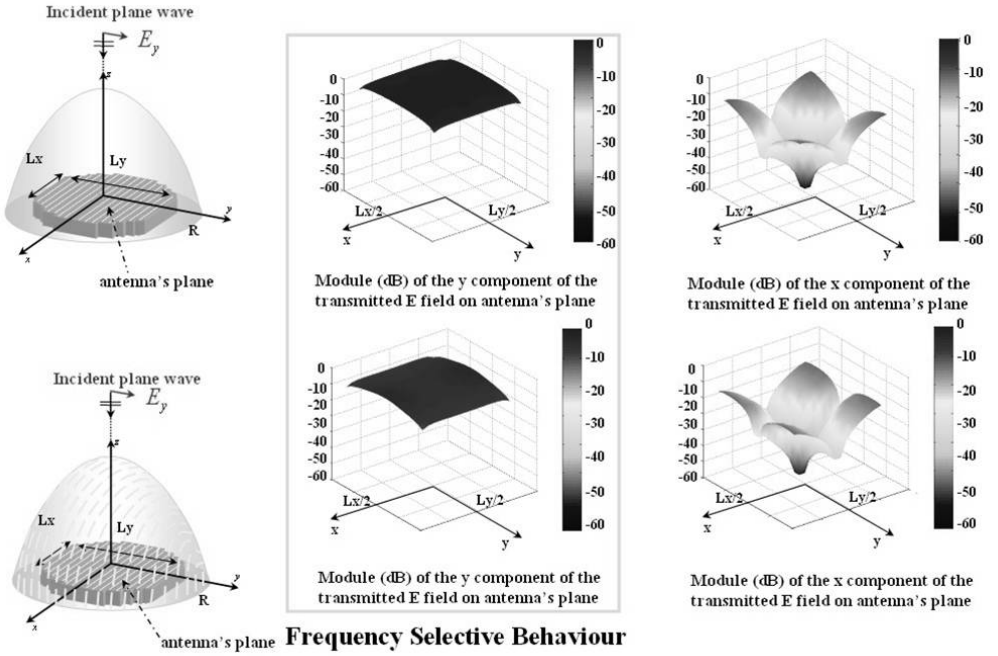

Fig. 11 Comparison between the module the electric field components transmitted on the antenna's plane by dielectric radome (upper part of the figure) and a FSS radome (lower part of the figure) for an impinging plane wave with electric field polarized along y direction (ortogonal to slot direction) at the frequency $0.75f_0$.

The radiation pattern of the antenna enclosed by the radome can be evaluated by the reaction integral between the equivalent currents on the antenna' s plane and the transmitted field. Numerical results are shown in Fig and Fig for the operating frequency f_0 and outside the pass-band at 0.75 f_0 respectively.

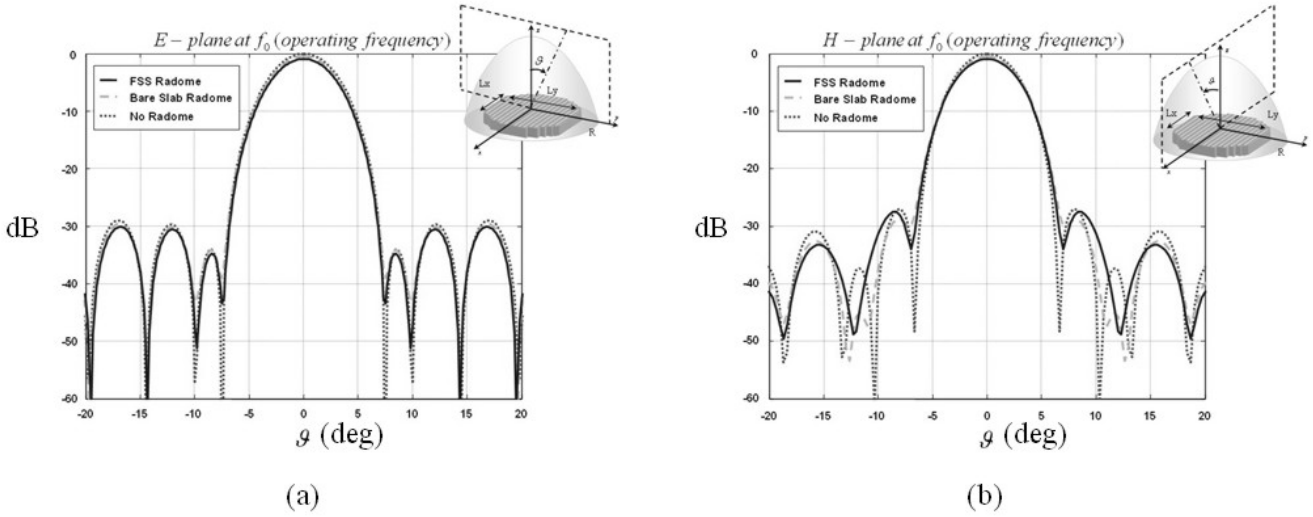

Fig. 12 (a) E-plane and (b) H-plane radiation pattern of the antenna at operating frequency f_0; dotted line refers to the radiation pattern of the antenna when it radiate in free space, dash-dotted line refers to the radiation pattern of the antenna enclosed by a dielectric radome and the continuous line refers to the radiation pattern of the antenna enclosed by the FSS radome.

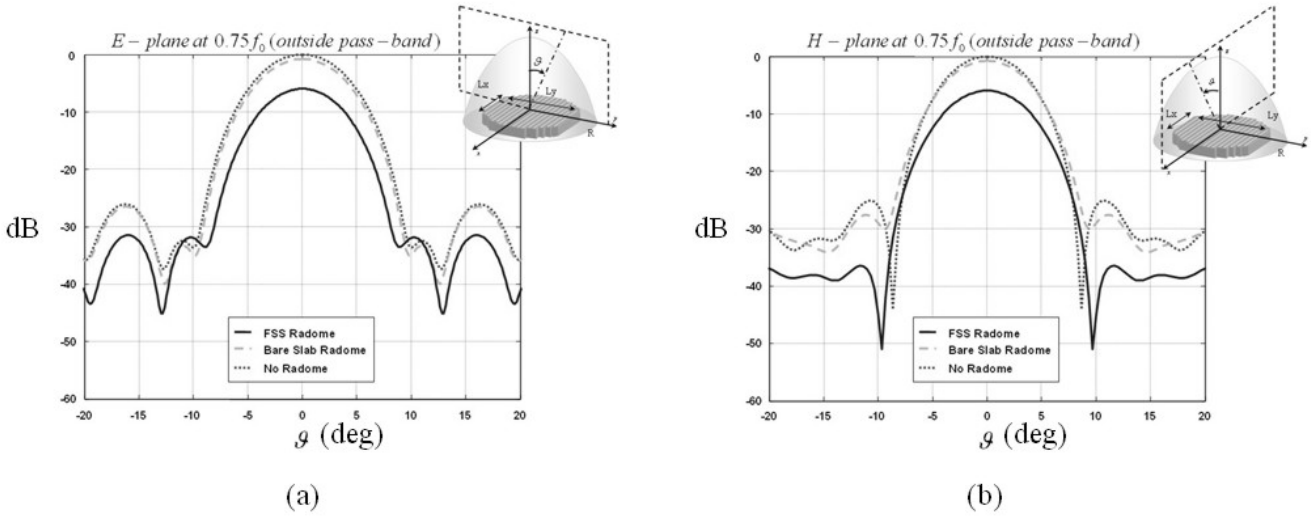

Fig. 13 (a) E-plane and (b) H-plane radiation pattern of the antenna at frequency 0.75 f_0 ouside the pass-band of the FSS; dotted line refers to the radiation pattern of the antenna when it radiate in free space, dash-dotted line refers to the radiation pattern of the antenna enclosed by a dielectric radome and the continuous line refers to the radiation pattern of the antenna enclosed by the FSS radome.

7.8 CONCLUSION

In this paper, a method for obtaining the analytical solution of the admittance (scattering) matrix of FSSs is presented. This method has been illustrated here with reference to a patch-type FSS or aperture-type FSS. On the basis of a spectral MoM solution, an equivalent network-matrix is defined with the ports corresponding to the accessible TE and TM FW of the exact Floquet expansion. The admittance matrix is then characterized by poles and residues associated to the matrix entries for a few values of the incidence angles. The identification of a set of surfaces associated with the poles and residue of the FSS and their regularity allows the interpolations of these surfaces by low-order polynomials. Network theory properties allow the approximation of the entries in terms of summation of rational functions. The consequent closed form expression is applied to evaluate the generalized scattering matrix as a function of the angle and polarization of incidence plane wave.

It is worth remarking that the full-wave analysis for each incident aspect (θ,ϕ) is very efficient, since it implies the inversion of a moderate size MoM matrix; however, obtaining accurate information on the continuous (θ,ϕ) domain requires a large amount of computational time. The main peculiarity of the method presented here is concerned with the possibility of reconstructing an analytical closed form the generalized scattering matrix in the continuous (θ,ϕ) domain over a large frequency range, starting from the response of the structure at a few samples. This is particularly useful to establish a link between an FSS solver and an HF solver for the analysis of large FSS curved structure or frequency selective radome no matter about the internal code solver structure. The general process described here can be applied for the synthetic description of different wave phenomena, like those relevant to surface wave propagation and electromagnetic band-gap description, near-field interaction (Green's function) and wave diffraction involving periodic surfaces.

References

[1] B.A. Munk, Frequency Selective Surfaces: Theory and Design, Wiley, New York, 2000.

[2] J. C. Vardaxoglou, Frequency selective surfaces, Research Studies Press Ltd., Taunton, England, 1997.

[3] P.-S. Kildal, "Artificially soft and hard surfaces in electromagnetics," IEEE Trans. Antennas Propagat. 38, 1537-1544, (1990).

[4] S. Maci and P.-S. Kildal, "Hard and soft gangbuster surfaces," Proceedings of the URSI International Symposium on Electromagnetic Theory, Pisa, Italy, May 23-27, 2004, URSI, Pisa, 2004, Vol. 2, pp. 290-292.

[5] M. Bozzi, S. Germani, L. Minelli, L. Perregrini, P. deMaagt, "Efficient calculation of the dispersion diagram of planar electromagnetic band-gap structures by the MoM/BI-RME method," IEEE Trans. Antennas Propagat., Special Issue on Artificial Magnetic Conductors, Soft/Hard Surfaces, and Other Complex Surfaces 53, 29-35, (2005).

[6] R. E. Collin, Foundations for microwave engineering, McGraw Hill, 1992.

[7] S. Maci, M. Caiazzo, A. Cucini, and M. Casaletti, "A pole-zero matching method for EBG surfaces composed of a dipole FSS printed on a grounded dielectric slab," IEEE Trans. Antennas Propagat., Special Issue on Artificial Magnetic Conductors, Soft/Hard Surfaces, and Other Complex Surfaces 53, 70-81, (2005).

[8] T. E. Rozzi, "Network analysis of strongly coupled transverse apertures in waveguide," Int. J. Circuit Theory Appl. 1, 161-178, (1973).

[9] E. A. Guillemin, Synthesis of Passive Networks, Robert E. Krieger Publishing Company, New York, 1977.